

# Investigation of TADF from a donor-acceptor compound with time-resolved fluorescence and DFT applying an optimally tuned range-separated hybrid functional

Reinhard Scholz,<sup>\*,†,§</sup> Paul Kleine,<sup>†</sup> Ramunas Lygaitis,<sup>†</sup> Ludwig Popp,<sup>†</sup> Simone Lenk,<sup>†</sup> Marc K. Etherington,<sup>¶</sup> Andrew P. Monkman,<sup>¶</sup> and Sebastian Reineke<sup>†</sup>

<sup>†</sup>*Dresden Integrated Center for Applied Physics and Photonic Materials (IAPP) and Institute for Applied Physics, Technische Universität Dresden, 01062 Dresden, Germany*

<sup>‡</sup>*Department of Organic Technology, Kaunas University of Technology, Radvilenu Plentas 19, LT 3028 Kaunas, Lithuania*

<sup>¶</sup>*OEM Research Group, Physics Department, Durham University, South Road, Durham DH1 3LE, United Kingdom*

<sup>§</sup>*Leibniz Institute of Polymer Research Dresden, P. O. Box 120 411, 01005 Dresden, Germany*

E-mail: reinhard.scholz@tu-dresden.de, scholz@ipfdd.de

## Abstract

Emitters showing thermally activated delayed fluorescence (TADF) in electroluminescent devices rely on efficient reverse intersystem crossing (rISC) arising for small thermal activation barriers between the lowest excited triplet and singlet manifolds. A small donor-acceptor compound consisting of a demethylacridine donor and a methylbenzoate acceptor group is used as a model TADF emitter. The spectroscopic signatures of this system are characterized using a combination of photoluminescence and photoluminescence excitation, and the decay dynamics between delays of 2 ns and 20 ms are recorded with time-resolved photoluminescence. Above  $T = 200$  K, our data provide convincing evidence for TADF at intermediate delays in the  $\mu\text{s}$  range, whereas triplet-triplet annihilation and slow triplet decay at later times can be observed over the entire temperature range from  $T = 80$  K to room temperature. Moreover, close to room temperature, we find a second and faster upconversion mechanism assigned to reverse internal conversion between different triplet configurations. An interpretation of these experimental findings requires a calculation of the deformation patterns and potential minima of several electronic configurations. This task is performed with range-separated hybrid functionals, outperforming standard density functionals or global hybrids. In particular, the systematic underestimate of the energy of charge transfer (CT) states with respect to local excitations within the constituting chromophores is replaced by more reliable transition energies for both kinds of excitations. Hence, several absorption and emission features can be assigned unambiguously, and the observed activation barriers for rISC and reverse internal conversion correspond to calculated energy differences between the potential surfaces in different electronic configurations.

## Introduction

Electronic devices relying on organic light-emitting diodes (OLEDs) have found widespread applications as displays for mobile phones and TV screens. Due to spin statistics, electron-hole pairs in electroluminescent devices form 25% singlet and 75% triplet excitons, so that

early fluorescent emitters were limited to an internal quantum efficiency (IQE) of one quarter. Together with an optical outcoupling efficiency around 20%, this corresponds to an external quantum efficiency (EQE) of about 5%.<sup>1,2</sup> For mobile devices and for general lighting applications of OLEDs, low power consumption relying on efficient emission processes becomes mandatory. Hence, several complementary strategies have been applied to a substantial improvement of the emission efficiency.

Attempts to harvest triplet excitons have started with phosphorescent molecules, where the large spin-orbit interaction at a heavy central metal ion like Ir facilitates radiative recombination of the triplet excitons.<sup>3</sup> For red and green emission, long-living phosphorescent materials with an IQE approaching 100% still represent the state of the art, and they are abundantly applied in commercial display applications. In principle, highly efficient blue phosphorescent emitters would allow for quite high power efficiencies of white OLEDs, but they suffer from photochemical instabilities and a rather short lifetime.<sup>4</sup> Moreover, the scarceness and price level of precious materials like Ir may result in economic constraints, inhibiting more widespread applications of OLED technology. These bottlenecks have resulted in tremendous research activities attempting to find other types of stable blue emitters with high quantum efficiency.

A complementary method to harvest triplet excitons relies on thermal excitation from the lowest triplet towards a higher-lying singlet potential surface via reverse intersystem crossing (rISC). rISC results from a thermally activated spin-flip process, governed by an Arrhenius-like temperature dependence.<sup>5</sup> Early developments of TADF emitters have concentrated on cationic complexes containing Cu(I),<sup>6,7</sup> later on generalized towards neutral emitters containing Sn(IV),<sup>8</sup> Cu(I),<sup>9</sup> and Ag(I).<sup>10</sup> As the respective emission processes involve charge transfer (CT) between metal and ligand, this concept was generalized to CT between purely organic donor and acceptor groups. A major breakthrough arose from the use of carbazole donors surrounding a dicyanobenzene acceptor core, allowing for an OLED with an impressive EQE of 19.4%.<sup>11</sup>

Meanwhile, optical transitions in molecular materials can be analyzed routinely with time-dependent density functional theory (TD-DFT). When comparing different pure density functionals in local density approximation (LDA) or generalized gradient approximation (GGA) with global hybrids, it turns out that a weight of 20% to 25% non-local Fock exchange minimizes the overall deviation from observed transition energies.<sup>12</sup> Smaller amounts of non-local exchange tend to underestimate observed transition energies, whereas hybrids with a larger fraction of non-local exchange overestimate them. In particular, the B3LYP hybrid functional<sup>13</sup> with 20% non-local Fock exchange has proven to yield quite reliable bond lengths, so that it has become particularly popular for DFT investigations of molecular materials.

However, when applying TD-DFT with well tested functionals to CT transitions, they result in systematic shortcomings, inhibiting a quantitative assignment. These problems of DFT and TD-DFT arise from the erroneous self-interaction of the electron, the resulting wrong asymptotics of the exchange-correlation functional towards large distance, and deviations of the derivative of the Kohn-Sham potential with respect to electron number from the discontinuity required for reproducing the correct gap between occupied and virtual states. Global hybrids like B3LYP alleviate some of these problems because the asymptotics of their exchange-correlation functionals rely on a fixed fraction of the Coulomb interaction, but a major part of the gap error remains.

It has already been known for a long time that exact non-local Fock exchange eliminates the asymptotic problems of CT states,<sup>14</sup> so that subsequent developments have attempted to reconcile this asymptotic requirement with the advantages of DFT for short distances. In applications of TD-DFT to inter- or intramolecular CT states, different strategies have emerged, allowing to adjust the amount of non-local exchange to the specific application.<sup>15-17</sup>

A generalization of DFT to range-separated hybrid functionals has proven to cure most of the systematic deviations observed for standard density functionals. In these hybrid approaches, the Coulomb interaction is partitioned into a short-range part treated in the

spirit of DFT, allowing to quantify electron correlation in a numerically efficient way, and a long-range part, treated with exact non-local Fock exchange.<sup>18–20</sup> A suitable range separation parameter can either be fixed globally for all applications like in the CAM-B3LYP functional,<sup>21</sup> or it can be deduced in a system-specific way by requiring a generalization of Koopmans’ theorem.<sup>22</sup> On this basis, it was demonstrated that intermolecular CT excitations can be calculated quite reliably.<sup>22</sup>

The application of similar range-separated hybrid schemes to TADF emitters has emerged only recently.<sup>23–31</sup> With respect to previous attempts to reconcile the advantages of DFT with correct Coulomb asymptotics for long distances, these methods are likely to provide a quantitative understanding of various essential ingredients of efficient TADF emitters, including *e.g.* the comparison between the performance of different functionals,<sup>24</sup> or the correlation between singlet-triplet splitting and transition dipole.<sup>25</sup> Small singlet-triplet splittings emerge for small spatial overlap between the frontier orbitals,<sup>26</sup> a correlation applied earlier to adapt the amount of non-local exchange to the degree of charge transfer.<sup>15</sup> Moreover, these range-separated hybrids allow to address the competition between different types of emission arising for different geometric conformers in a meaningful way.<sup>23,28</sup>

In the present work, we describe a comprehensive spectroscopic characterization of a TADF model compound, and we interpret the experimental findings with detailed density functional calculations relying on a carefully chosen range-separated hybrid functional. Sec. summarizes basic requirements for good TADF emitters and presents the synthesis of our model compound. The experimental methods are described in Sec. before discussing the photophysics of our TADF emitter in Sec. . In Sec. , we introduce an optimally tuned range-separated variant of the global hybrid functional B3LYP<sup>13</sup> and apply it to our model compound. Sec. interprets the experimental findings with the DFT results described in Sec. , and Sec. summarizes the present achievements.

# TADF model compound: DMAC-MB

## Minimizing singlet-triplet splitting

A key parameter for an efficient rISC process is a sufficiently small activation energy  $\Delta_{\text{ST}}$  from the lowest triplet configuration  $T_1$  to the lowest excited singlet  $S_1$ . This splitting relies on the exchange interaction between the two orbitals involved, usually the highest occupied molecular orbital (HOMO,  $\Phi_{\text{H}}$ ) and the lowest unoccupied orbital (LUMO,  $\Phi_{\text{L}}$ ), which can be expressed as the Coulomb interaction of the overlap charge density  $\rho_{\text{HL}}(\mathbf{r}) = \Phi_{\text{H}}(\mathbf{r})\Phi_{\text{L}}(\mathbf{r})$  with itself,

$$J = \int d^3r_1 \int d^3r_2 \rho_{\text{HL}}(\mathbf{r}_1) \frac{e^2}{4\pi\epsilon_0|\mathbf{r}_1 - \mathbf{r}_2|} \rho_{\text{HL}}(\mathbf{r}_2). \quad (1)$$

Hence, a minimization of the exchange integral  $J$  and the singlet-triplet splitting  $\Delta_{\text{ST}} = 2J$  corresponds to a minimization of the overlap charge density  $\rho_{\text{HL}}$  *everywhere* in space. This optimization criterion is in clear contradiction to a further mandatory ingredient for an efficient emitter, consisting in a transition dipole  $\boldsymbol{\mu}$  of acceptable size,

$$\boldsymbol{\mu} = e\langle\Phi_{\text{H}}|\mathbf{r}|\Phi_{\text{L}}\rangle = e \int d^3r \mathbf{r} \rho_{\text{HL}}(\mathbf{r}), \quad (2)$$

governing in turn the radiative recombination rate of singlet excitons, scaling as the square of the transition dipole.<sup>32</sup>

An efficient minimization of overlap charge density and exchange integral can be achieved by localizing the HOMO mainly on a donor group, and the LUMO mainly on an acceptor. Furthermore, a hybridization between  $\pi$  frontier orbitals on different groups can be reduced further if steric hindrance around the donor-acceptor bond enforces a close to orthogonal orientation of the respective aromatic planes. Hence, the accepted main paradigm for achieving efficient TADF emitters consists in a maximized dihedral angle between donor and acceptor. Of course, as argued above, the beneficial small singlet-triplet splitting sacrifices the transition dipole. According to El Sayed’s rule, such an idealized geometric arrangement has

also a detrimental influence on the spin-orbit matrix elements required for the rISC spin-flip process.

In practice, even in such an idealized orthogonal arrangement, these disadvantages are alleviated by thermal motion, involving in particular changes in the dihedral angle. The resulting thermal distribution of geometries speeds up each of the processes required for an efficient TADF emitter. Concerning the radiative recombination rate of our model compound, this topic will be addressed again in Sec. .

## Synthesis of model compound

Our model compound Methyl 2-(9,9-dimethylacridin-10-yl)benzoate (DMAC-MB) relies on the well established donor group 9,9-Dimethyl-9,10-dihydroacridine (DMAC)<sup>33-35</sup> and an acceptor-functionalized phenyl group realized in the form of methylbenzoate (MB), compare Fig. 1. 9,9-Dimethyl-9,10-dihydroacridine (DMAC) was synthesized according the procedures described elsewhere.<sup>36,37</sup> Methyl-2-iodobenzoate was synthesized via a cost efficient synthetic route.<sup>38</sup> Methyl anthranilate (98%) was purchased from Fluka and used as received, and dichlorobenzene was re-distilled before usage.

9,9-Dimethyl-9,10-dihydroacridine (1 g, 4.8 mmol), methyl-2-iodobenzoate (1.25 g, 4.8 mmol), activated  $K_2CO_3$  (0.66 g, 4.8 mmol) and dichlorobenzene (25 ml) were placed into a 100 ml Schlenk flask. The reaction mixture was de-oxygenated several times using a membrane pump before adding Cu (0.61 g, 9.6 mmol) and CuI (0.036 g, 0.19 mmol) under  $N_2$  atmosphere. The reaction mixture was stirred at 190°C for 24 h. Afterwards it was filtered, and the remaining solid was washed with toluene and tetrahydrofuran. The filtrate was concentrated under reduced pressure. The raw product was purified by column chromatography using a chloroform:hexane = 1:1 mixture as eluent. The purification yielded 0.95 g of yellow crystalline material (58%) (melting point 169°C obtained by DSC at a heating rate of 5°C/min). The material obtained was purified twice by sublimation, applying a temperature gradient under high vacuum conditions.

Further information on nuclear magnetic resonance (NMR) spectra is given in the Supplementary Material.

## Molecular geometry

Around the phenyl group, the *ortho* configuration of the ester functionalization with respect to the bond towards the DMAC donor maximizes the steric hindrance between the two aromatic groups, stabilizing an orthogonal dihedral angle between them.

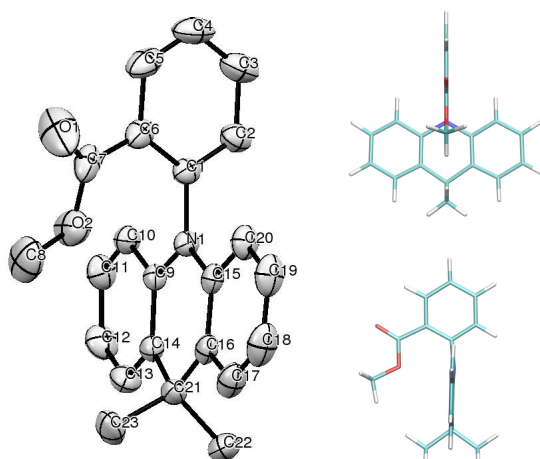


Figure 1: Left: ORTEP view (50% probability level) of the DMAC-MB structure in the crystalline phase, drawn using Mercury software. H-atoms have been omitted for clarity. Right:  $C_s$  symmetric geometry of free DMAC-MB, optimized with an optimally tuned range-separated hybrid functional discussed in Sec. , seen along the normal of the DMAC donor group (top), and along the normal of the MB acceptor group (bottom).

In the crystalline phase, the methoxy group is oriented towards the direction of the DMAC donor, like in the most stable form of the free molecule, but intermolecular interactions change the dihedral angle between donor and acceptor from right angle in the free molecule ( $C_s$  point group) to an average value of  $79.8^\circ$  ( $75.9^\circ$  towards carboxylate group,  $83.7^\circ$  towards

opposite part of phenyl ring).

CCDC-1558854 contains details of the crystallographic data reported in this paper.<sup>39</sup> Further information on the crystal structure is given in the Supplementary Material.

## Experimental methods

### Sample preparation

Host-guest films were prepared in zeonex (Cyclo Olefin Polymer) by drop casting a solution of the polymer onto glass substrates with a ratio of 5 wt% of the active substance dissolved in toluene. Besides this diluted 5 wt.% DMAC-MB:zeonex sample, further spectroscopic measurements will address an amorphous neat film of DMAC-MB and a sample consisting of crystalline needles.

### Optical characterization

For detailed steady-state photoluminescence measurements on the three types of DMAC-MB samples, a Spex FluoroMax spectrofluorometer has been used. The excitation scans were performed while recording the emission at 500 nm. UV/VIS absorption profiles were measured on a Shimadzu UV-3100 UV-VIS-NIR system. Steady-state photoluminescence measurements were performed using a mounted UV-LED (Thorlabs M365L2) with excitation at 365 nm (3.40 eV), using an additional bandpass filter (Thorlabs FB370-10) with central wavelength at  $(370 \pm 2)$  nm and FWHM of  $(10 \pm 2)$  nm.

The photoluminescence quantum yield was measured in an integrating sphere continuously purged by nitrogen via de Mello's method.<sup>40</sup> Using a CAS 140 CT spectrometer (Instrument Systems) and the 365 nm (3.40 eV) excitation source (Thorlabs M365L2), the quantum yield measurement was corrected via its reabsorption, and averaged over 5 iterations.

## Time-resolved PL spectroscopy

Temperature-dependent transient PL measurements were acquired using a liquid nitrogen cryostat (Janis Research). Prompt fluorescence (PF), delayed emission (DF) spectra and phosphorescence decays were recorded by nanosecond gated luminescence measurements (covering the range between 400 ps to 1 s).

The sample was excited by the third harmonic of a Nd:YAG laser at 355 nm (EKSPLA), and the emission was detected with a sensitive gated iCCD camera (Stanford Computer Optics), after passing a spectrograph. Measurements were controlled by exponentially increasing gate and delay times.<sup>41</sup>

For laser fluence measurements on DMAC-MB, an additional N<sub>2</sub> laser emitting at 337 nm was used, while the excitation density was controlled with a density filter wheel within the optical path.

## Photophysics of DMAC-MB

### Decay dynamics

In photoluminescence, singlet states can directly be excited via a laser pulse, decaying subsequently via a radiative fluorescence rate  $k_{S,\text{rad}}$ , a non-radiative rate  $k_{S,\text{nr}}$ , and an intersystem crossing (ISC) rate  $k_{\text{ISC}}$  towards the triplet manifold, with an overall singlet decay rate

$$k_S = k_{S,\text{rad}} + k_{S,\text{nr}} + k_{\text{ISC}}. \quad (3)$$

Triplet states are created via ISC, and they decay with a radiative phosphorescence rate,  $k_{T,\text{rad}}$ , a non-radiative rate  $k_{T,\text{nr}}$ , and a reverse intersystem crossing (rISC) rate  $k_{\text{rISC}}$ , resulting in a triplet decay rate

$$k_T = k_{T,\text{rad}} + k_{T,\text{nr}} + k_{\text{rISC}}. \quad (4)$$

In the linear regime, the densities of excited singlets and triplets,  $n_S(t)$  and  $n_T(t)$ , are governed by a set of coupled linear differential equations,

$$\frac{d}{dt} \begin{pmatrix} n_S \\ n_T \end{pmatrix} = \begin{pmatrix} -k_S & k_{\text{rISC}} \\ k_{\text{ISC}} & -k_T \end{pmatrix} \begin{pmatrix} n_S \\ n_T \end{pmatrix}. \quad (5)$$

The two eigenvectors decay exponentially with a rate  $k_{\text{pf}}$  for prompt fluorescence and  $k_{\text{df}}$  for delayed fluorescence,

$$k_{\text{pf,df}} = \frac{k_S + k_T}{2} \pm \frac{k_S - k_T}{2} \sqrt{1 + 4 \frac{k_{\text{ISC}} k_{\text{rISC}}}{(k_S - k_T)^2}}. \quad (6)$$

Due to  $k_{\text{rISC}}, k_T \ll k_S$ , the square root can be approximated by its first order Taylor series expansion, resulting in the following rates for prompt and delayed fluorescence

$$k_{\text{pf}} = k_S + \frac{k_{\text{ISC}} k_{\text{rISC}}}{k_S} \quad (7)$$

$$k_{\text{df}} = k_T - \frac{k_{\text{ISC}} k_{\text{rISC}}}{k_S} \quad (8)$$

where the denominator in eq. (6) has been approximated as  $k_S - k_T \approx k_S$ .

The set of linear differential equations (5) can only result in exponentially decaying solutions with rates according to eq. (6) or its approximate form eqs. (7,8). However, at long delays, the fluorescence intensity of DMAC-MB presented below gives clear evidence for a decay proportional to  $t^{-n}$  with an exponent  $n$  in the range between 1 and 2. Such a decay can be derived from the following set of non-linear differential equations accounting for triplet-triplet annihilation (TTA) of two triplets towards an excited singlet and a ground state singlet,  $T_1 + T_1 \rightarrow S_n + S_0$ :

$$\frac{d}{dt} n_S = -k_S n_S + k_{\text{ISC}} n_T + \frac{1}{2} k_{\text{TTA}} n_T^2 \quad (9)$$

$$\frac{d}{dt} n_T = k_{\text{ISC}} n_S - k_T n_T - k_{\text{TTA}} n_T^2 \quad (10)$$

where the excited singlet  $S_n$  is assumed to relax towards the lowest excited singlet  $S_1$  via fast internal conversion, so that the balance equations (9,10) address the lowest excited configurations,  $S_1$  and  $T_1$ . Neglecting the small change of the triplet density during the fastest time scale  $1/k_S$  occurring in these equations, eq. (9) results simply in

$$n_S = \frac{k_{\text{rISC}}}{k_S} n_T + \frac{k_{\text{TTA}}}{2k_S} n_T^2 \quad (11)$$

so that the differential equation for the triplets reads

$$\frac{d}{dt} n_T = -K_T n_T - K_{\text{TTA}} n_T^2, \quad (12)$$

with the abbreviations

$$K_T = \left( 1 - \frac{k_{\text{ISC}}}{k_S} \frac{k_{\text{rISC}}}{k_T} \right) k_T \quad (13)$$

$$K_{\text{TTA}} = \left( 1 - \frac{k_{\text{ISC}}}{2k_S} \right) k_T \quad (14)$$

As expected,  $K_T$  reproduces the decay rate  $k_{\text{df}}$  of delayed fluorescence according to eq. (8).

The nonlinear differential equation (12) is solved by

$$n_T = \frac{n_0}{\left( 1 + \frac{K_{\text{TTA}} n_0}{K_T} \right) e^{K_T t} - \frac{K_{\text{TTA}} n_0}{K_T}}. \quad (15)$$

In the following, this decay regime will be discussed for the case of a long-living reservoir of triplets which can not return to the singlet manifold via efficient rISC processes. Hence, triplets can only decay to the electronic ground state  $S_0$  via phosphorescence or non-radiative decay, and it turns out that the triplet decay rate  $K_T = k_T$  becomes slower than the maximum delay range in the experimental set-up of 10 ms. Under these conditions,  $t \ll 1/K_T$ ,

a linearization of the exponential

$$e^{K_{\text{T}}t} \approx 1 + K_{\text{T}}t \quad (16)$$

results in a seemingly algebraic decay over the delay range of interest

$$n_{\text{T}} \approx \frac{n_0}{1 + (K_{\text{T}} + K_{\text{TTA}}n_0)t}, \quad (17)$$

an approximation which has already been applied to slow triplet decay under similar conditions.<sup>42</sup> According to eq. (11), the singlet density  $n_{\text{S}}$  will respond with terms proportional to  $n_{\text{T}}$  and to  $n_{\text{T}}^2$ , resulting in a fluorescence intensity proportional to

$$I_{\text{fl}} \propto k_{\text{S,rad}} \left( \frac{k_{\text{rISC}}}{2k_{\text{S}}} n_{\text{T}} + \frac{k_{\text{TTA}}}{2k_{\text{S}}} n_{\text{T}}^2 \right), \quad (18)$$

whereas the phosphorescence intensity would scale with the first power of the triplet density,

$$I_{\text{ph}} \propto k_{\text{T,rad}} n_{\text{T}}. \quad (19)$$

For short times  $t < 1/k_{\text{S}}$ , intersystem crossing did not produce substantial amounts of triplets yet, so that interpolating eq. (15) back towards zero delay remains approximate. The solution of the set of linear differential equations in eq. (5) reveals that at short times, the triplet density grows proportional to  $[e^{-k_{\text{af}}t} - e^{-k_{\text{pf}}t}]$ , compare Ref.<sup>29</sup> for a visualization.

However, even at longer delays, fluorescence and phosphorescence contributions according to eqs. (18,19) remain much smaller than the prompt and delayed fluorescence governed by ISC and rISC, so that an interpolation of these smaller contributions with eqs. (18,19) towards short delays does not have a significant influence on the determination of other decay parameters.

**Table 1: Photoluminescence quantum yield at room temperature ( $T = 300$  K): Total photoluminescence quantum yield  $\Phi_{\text{PL}}$  measured in an integrating sphere, and contributions  $\Phi_{\text{pf}}$  from prompt and  $\Phi_{\text{df}}$  from delayed fluorescence, respectively, deduced from time-resolved PL, compare Sec. .**

	$\Phi_{\text{PL}}$ %	$\Phi_{\text{pf}}$ %	$\Phi_{\text{df}}$ %
5 wt.% film	$93 \pm 1$	$9 \pm 1$	$84 \pm 1$
neat film	$63 \pm 6$		
crystal	$60 \pm 1$	$49 \pm 1$	$11 \pm 1$

## Photoluminescence quantum yield

Three types of samples will be discussed in the following: A film of 5wt% DMAC-MB embedded in an olefin polymer matrix (zeonex), an amorphous neat film of DMAC-MB, and an assembly of crystalline needles. The diluted sample shows a photoluminescence quantum yield (PLQY) of  $\Phi_{\text{PL}} = 93 \pm 1$  %, decreasing over  $63 \pm 6$  % for the amorphous neat film towards  $60 \pm 1$  % for the crystalline sample, compare Table 1.

In particular in the diluted sample, the very high PLQY makes it rather unlikely that both singlets and triplets can decay non-radiatively to the electronic ground state with significant decay rates  $k_{\text{S,nr}}$  and  $k_{\text{T,nr}}$ , respectively. In addition, from the very slow decay at delay times beyond 1 ms discussed in Sec. , a long-living triplet species not taking part in TADF decays towards the ground state with a rate  $k_{\text{T}} = k_{\text{T,rad}} + k_{\text{T,n}} < 10^2 \text{ s}^{-1}$ , and there is no specific reason why the triplets promoting TADF should have larger decay rates towards the ground state. Hence, a convenient approximation allowing to determine the six rates contributing to eqs. (3,4) consists in assuming  $k_{\text{T,r}} = k_{\text{T,nr}} = 0$ , so that the triplet decay rate reduces to  $k_{\text{T}} = k_{\text{rISC}}$ , and the rISC yield becomes unity,  $\Phi_{\text{rISC}} = k_{\text{rISC}}/k_{\text{T}} = 1$ . This simplifies the

total and fractional PLQY to

$$\Phi_{\text{PL}} = \frac{k_{\text{S,r}}}{k_{\text{S,r}} + k_{\text{S,nr}}} \quad (20)$$

$$\Phi_{\text{pf}} = \frac{k_{\text{S,r}}}{k_{\text{S}}} \quad (21)$$

$$\Phi_{\text{df}} = \Phi_{\text{pf}} \frac{\Phi_{\text{ISC}}}{1 - \Phi_{\text{ISC}}} \quad (22)$$

with the abbreviation  $\Phi_{\text{ISC}} = k_{\text{ISC}}/k_{\text{S}}$ .<sup>43</sup>

Using the tabulated values of  $\Phi_{\text{pf}}$  and  $\Phi_{\text{df}}$ , the efficiency of the ISC process can be determined from the ratio between the yields of prompt and delayed fluorescence,

$$\Phi_{\text{ISC}} = \frac{1}{1 + \frac{\Phi_{\text{pf}}}{\Phi_{\text{df}}}}, \quad (23)$$

giving  $\Phi_{\text{ISC}} \approx 0.9$  for the 5 wt.% film, i.e. singlet decay is by far dominated by intersystem crossing.

## Fluorescence decay

For the diluted sample with 5 wt.% in zeonex, Fig. 2 reports the spectrally integrated fluorescence intensity as a function of delay after the excitation pulse. For all temperatures in the range  $T = 80$  K to  $T = 300$  K, the transients give clear evidence for prompt fluorescence dominating over the first 100 ns, and a slow decay at very long delays, governed by a power law  $I(t) \propto t^{-n}$ , with an exponent  $n$  in the range  $1 \leq n \leq 2$ . Up to a temperature of  $T = 180$  K, the decay traces show no significant contribution of delayed fluorescence arising from rISC processes, but TADF via rISC sets in at  $T = 200$  K and above.

The decay of the fluorescence intensity in Figs. 2 and 3 was analysed with a combination of prompt fluorescence, delayed fluorescence, and the decay of a long-living triplet population  $n_{\text{T}}$  not taking part in TADF via rISC, resulting in fluorescence proportional to  $n_{\text{T}}$  and to  $n_{\text{T}}^2$ , and to phosphorescence proportional to  $n_{\text{T}}$ , compare eqs. (18,19). The slowest decay at

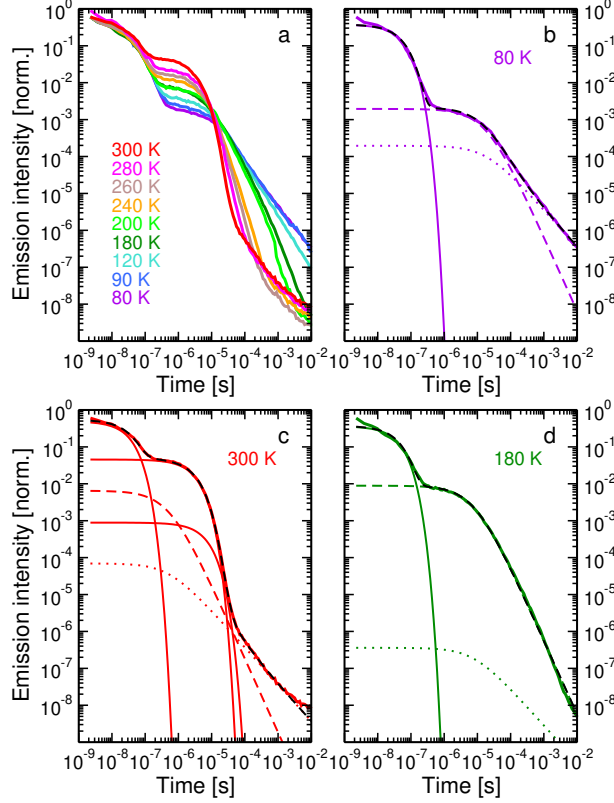


Figure 2: Spectrally integrated fluorescence intensity as a function of delay after the excitation pulse, measured on a 5 wt.% zeonex:DMAC-MB film, and data analysis for selected temperatures, using a combination of prompt fluorescence, delayed fluorescence, and fluorescence and phosphorescence arising from the slow decay of triplets not taking part in TADF via rISC. (a) Decay traces for different temperatures in the range from  $T = 80$  K to  $T = 300$  K, (b) data analysis for  $T = 80$  K, (c) for  $T = 300$  K, and (d) for  $T = 180$  K. In (b,d), the decay model includes prompt fluorescence and fluorescence arising from non-linear triplet decay for longer delay times, whereas (c) contains two additional channels of delayed fluorescence. Exponentially decaying components are shown as solid lines, fluorescence proportional to  $n_T^2$  as dashed lines, and fluorescence or phosphorescence proportional to  $n_T$  as dotted lines. The overall fits are superimposed on the measured data as black dashed lines.

long delays remains close to algebraic,  $t^{-n}$ , so that the decay rate of the triplets  $K_T$  has to be slower than the longest delay range. For this reason, this rate was fixed to a sufficiently slow value,  $K_T = 1 \text{ s}^{-1}$ .

At temperatures below  $T = 180$  K, the entire delay range can be interpreted allowing for prompt fluorescence and fluorescence according to eqs. (18,19), but excluding TADF, compare Fig. 2b for  $T = 80$  K and Fig. 2d for  $T = 180$  K. In the temperature range from  $T = 200$  K to  $T = 300$  K where TADF becomes important, it turned out that the fit

improved substantially when allowing for two different contributions to delayed fluorescence, presumably arising from molecules with different geometric constraints induced by the embedding into the polymer film. The fitted decay rates of prompt and delayed fluorescence are summarized in Table 2.

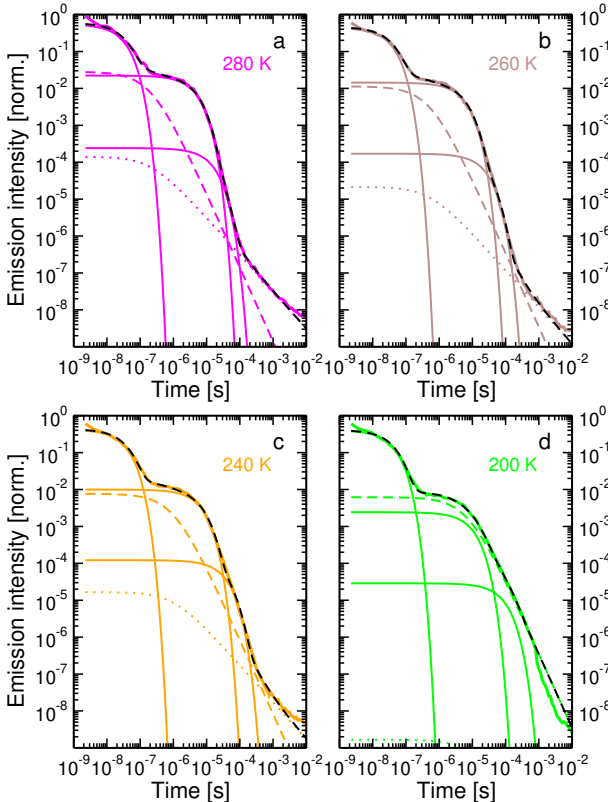


Figure 3: Analysis of fluorescence intensity as a function of delay after the excitation pulse, measured on a 5 wt.% zeonex:DMAC-MB film, for temperatures of (a)  $T = 280$  K, (b)  $T = 260$  K, (c)  $T = 240$  K, and (d)  $T = 200$  K. Line code as in Fig. 2.

As an example, Fig. 2c shows the decomposition of the intensity decay at room temperature ( $T = 300$  K), giving clear evidence for exponentially decaying delayed fluorescence in the time range from about 100 ns to 100  $\mu$ s. In order to achieve a fit with similar *relative* precision over many orders of magnitude in delay and intensity, the fit was performed for the logarithm of intensity,  $\log I$ . At  $10^{-8}$  of the initial intensity, the detection system approaches its noise level, so that the recorded intensity starts to deviate upwards from any reasonable fitting function. When the signal quality allowed, the fit was performed up to a time delay of 2.2 ms, excluding  $T = 200$  K, where the observed fluorescence intensity drops in an

uncontrolled fashion for  $t > 1$  ms, so that the time range was limited to a delay of 0.7 ms. For very short delay  $t < 5$  ns, the measured data show some evidence for a faster decaying component, which was not represented by a respective decay channel in our intensity model. At  $T = 280$  K, this systematic deviation between model function and data resulted in an undesirable drift of the fitting parameters, forcing us to exclude the very first delay time of 2.25 ns from the data analysis.

## Dependence of delayed fluorescence on excitation intensity

At room temperature, the time-integrated delayed PL intensity of a 5 wt.% zeonex:DMAC-MB film was recorded for different excitation intensities. As shown in Fig. 4a, within a delay range from 1  $\mu$ s to 81  $\mu$ s, the integrated delayed fluorescence depends essentially linearly on the excitation power, with a power law governed by a slope of  $1.03 \pm 0.02$ . This indicates a single photon up-conversion mechanism, consistent with a TADF process promoted via thermally activated rISC. Instead, triplet-triplet annihilation (TTA) would rely on a two particle collision process, giving rise to a strictly quadratic dependence.<sup>44</sup> This limits the contribution of TTA in the delay range 1  $\mu$ s to 81  $\mu$ s to a few percent.

## Activation barriers for rISC

In a temperature regime where thermal activation promotes the rISC process, triplet states decay preferentially via rISC, so that the decay rate of delayed fluorescence according to the approximate relation eq. (8) becomes

$$k_{\text{df}} = k_{\text{rISC}} \left( 1 - \frac{k_{\text{ISC}}}{k_{\text{S}}} \right). \tag{24}$$

Due to the very high ISC efficiency  $\Phi_{\text{ISC}} = k_{\text{ISC}}/k_{\text{S}} \approx 0.9$  determined from the observed PLQY via eqs. (21-23), the rISC rate  $k_{\text{rISC}}$  is about ten times faster than the resulting decay rate  $k_{\text{df}}$  of delayed fluorescence.

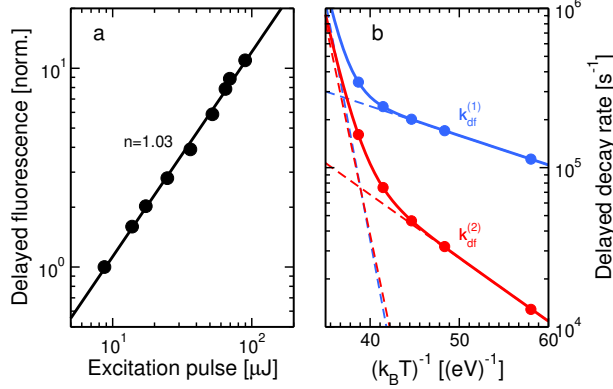


Figure 4: (a) Dependence of delayed fluorescence on excitation power (dots), and fit with a power law, giving an exponent of  $1.03 \pm 0.02$ . The experimental points have been obtained from a time integration of the delayed fluorescence from a delay of  $1 \mu\text{s}$  to  $81 \mu\text{s}$ . (b) Decay rates of delayed fluorescence on a logarithmic scale, and fit with an Arrhenius dependence relying on two different activation energies. Dots: decay rates  $k_{\text{df}}^{(1)}$  and  $k_{\text{df}}^{(2)}$  of delayed fluorescence as tabulated in Table 2, linear slopes (dashed) for each temperature-activated process, thick coloured lines: fit according to eq. (25). The Arrhenius fit results in activation barriers of  $43 \pm 1 \text{ meV}$  and  $0.69 \pm 0.02 \text{ eV}$  for the faster process  $k_{\text{df}}^{(1)}$ , and of  $92 \pm 3 \text{ meV}$  and  $0.61 \pm 0.03 \text{ eV}$  for the slower one,  $k_{\text{df}}^{(2)}$ .

The observed fluorescence decay rates are reported in Table 2 and visualized in Fig. 4b, revealing that each of the two delayed fluorescence channels  $k_{\text{df}}^{(1)}$  and  $k_{\text{df}}^{(2)}$  speeds up at higher temperature. For each of these temperature-dependent decay rates, we assume a combination

**Table 2: Decay rates fitted to the measured time dependence of the spectrally integrated fluorescence intensity in Figs. 2,3: decay of prompt fluorescence  $k_{\text{pf}}$ , and two rates  $k_{\text{df}}^{(1)}$  and  $k_{\text{df}}^{(2)}$  contributing to delayed fluorescence.**

T	$k_{\text{B}}T$	$(k_{\text{B}}T)^{-1}$	$k_{\text{pf}}$	$k_{\text{df}}^{(1)}$	$k_{\text{df}}^{(2)}$
K	meV	$(\text{eV})^{-1}$	$\text{s}^{-1}$	$\text{s}^{-1}$	$\text{s}^{-1}$
300	25.85	38.68	$3.17 \times 10^7$	$3.45 \times 10^5$	$1.61 \times 10^5$
280	24.13	41.45	$3.42 \times 10^7$	$2.42 \times 10^5$	$7.50 \times 10^4$
260	22.40	44.64	$3.04 \times 10^7$	$2.01 \times 10^5$	$4.63 \times 10^4$
240	20.68	48.36	$2.98 \times 10^7$	$1.71 \times 10^5$	$3.20 \times 10^4$
200	17.23	58.03	$2.56 \times 10^7$	$1.13 \times 10^5$	$1.29 \times 10^4$

of two different activation processes, each governed by an Arrhenius dependence,

$$k_{\text{df}}^{(j)} = k_1^{(j)} \exp\left(-\frac{E_{\text{act},1}^{(j)}}{k_{\text{B}}T}\right) + k_2^{(j)} \exp\left(-\frac{E_{\text{act},2}^{(j)}}{k_{\text{B}}T}\right) \quad (25)$$

allowing to deduce the respective activation barriers for each of the two delayed channels  $j = 1$  or  $j = 2$ .

The faster rate  $k_{\text{df}}^{(1)}$  with the much larger intensities in Figs. 2,3 reveals a low-temperature activation energy of  $43 \pm 1$  meV, and the slower rate  $k_{\text{df}}^{(2)}$  a low-temperature activation energy of  $95 \pm 2$  meV, whereas both rates indicate a faster high-temperature process governed by much larger activation energies of  $0.69 \pm 0.02$  eV and  $0.61 \pm 0.03$  eV, respectively.

Based on the DFT calculations in Sec. , the small low-temperature activation barrier will be assigned to rISC, and the large high temperature activation barrier to reverse internal conversion (rIC) from a  $^3\text{CT}$  triplet to an acceptor triplet  $^3\text{A}$  with subsequent barrierless and fast rISC towards  $S_1$ , compare Sec. for further details.

Close to room temperature, the presence of two distinct up-conversion processes requires a generalization of the linear decay regime, eq. (5). Due to the high PLQY, it remains reasonable to assume that triplets cannot decay directly to the electronic ground state, but we allow for both up-conversion processes deduced from Fig. 4:

$$k_{\text{T}} = k_{\text{rISC}} + k_{\text{rIC}}. \quad (26)$$

Under these assumptions, and fast rISC from  $^3\text{A}$  towards  $S_1$ , both types of up-conversion generate radiative  $S_1$  states, as observed via delayed fluorescence. Therefore, diagonal and off-diagonal entries to the matrix governing linear decay have to include both processes in

eq. (26), abbreviated for simplicity as  $k_T$ :

$$\frac{d}{dt} \begin{pmatrix} n_S \\ n_T \end{pmatrix} = \begin{pmatrix} -k_S & k_T \\ k_{\text{ISC}} & -k_T \end{pmatrix} \begin{pmatrix} n_S \\ n_T \end{pmatrix}. \quad (27)$$

so that the two observed fluorescence decay rates become

$$k_{\text{pf,df}} = \frac{k_S + k_T}{2} \pm \frac{k_S - k_T}{2} \sqrt{1 + 4 \frac{k_{\text{ISC}} k_T}{(k_S - k_T)^2}}. \quad (28)$$

Among the ingredients of the off-diagonal elements in eq. (27), we can relate ISC and rISC processes by the Arrhenius barrier obtained from the data analysis in Fig. 4,

$$\frac{k_{\text{rISC}}}{k_{\text{ISC}}} = \exp \left( -\frac{E_{\text{act},1}^{(1)}}{k_B T} \right), \quad (29)$$

allowing to express  $k_{\text{rISC}}$  in eq. (26) accordingly. In the following, we will deduce all rates governing the more prominent delayed channel, with an overall decay rate of  $k_{\text{df}}^{(1)} = 3.45 \times 10^5 \text{ s}^{-1}$  at  $T = 300 \text{ K}$ , compare Table 2. The Arrhenius fit in Fig. 4 allows to assign  $k_{\text{df,rISC}} = 2.57 \times 10^5 \text{ s}^{-1}$  and  $k_{\text{df,rIC}} = 0.87 \times 10^5 \text{ s}^{-1}$  to the two types of up-conversion processes, with a ratio corresponding to the ratio of the underlying processes,  $k_{\text{rISC}}$  and  $k_{\text{rIC}}$ , so that each of them can be expressed by the still unknown  $k_{\text{ISC}}$ . The remaining rather tedious task is to derive  $k_{\text{ISC}}$  from a quadratic equation deduced from suitable combinations of the solutions of eq. (28).

This procedure results in a singlet decay rate of  $k_S = 2.58 \times 10^7 \text{ s}^{-1}$ , a radiative recombination rate of  $k_{\text{S,rad}} = 0.16 \times 10^7 \text{ s}^{-1}$ , a non-radiative decay rate of  $k_{\text{S,nr}} = 1.2 \times 10^5 \text{ s}^{-1}$ , an ISC rate of  $k_{\text{ISC}} = 2.41 \times 10^7 \text{ s}^{-1}$ , a rISC rate of  $k_{\text{rISC}} = 0.46 \times 10^7 \text{ s}^{-1}$ , and a rate  $k_{\text{rIC}} = 0.16 \times 10^7 \text{ s}^{-1}$  for reverse internal conversion to a higher lying triplet configuration with subsequent fast rISC towards  $S_1$ . The ordering  $k_{\text{rISC}} > k_{\text{S,rad}}$  may seem somewhat surprising for an efficient emitter, but this underlines once more that a carefully designed

TADF compound promotes quite fast rISC processes, without compromising a high PLQY.

## Emission lineshapes

Neglecting the deformation of a molecule in its relaxed excited geometry, the radiative recombination rate from an excited singlet  $S_1$  back to the ground state  $S_0$  can be written as

$$k_{S,\text{rad}} = \frac{\boldsymbol{\mu}^2 E^3 n^3}{3\pi\epsilon_0 \hbar^4 c^3} \quad (30)$$

where  $\boldsymbol{\mu}$  is the transition dipole vector,  $E$  the transition energy, and  $n$  the refractive index of the surrounding medium.<sup>32</sup> Due to the molecular deformation, this expression has to be generalized to a sum over transitions from the lowest vibrational level  $|\psi_{e0}\rangle$  in the excited potential to different vibrational levels  $|\psi_{gj}\rangle$  in the electronic ground state. In the Born-Oppenheimer approximation, each state factorizes into an electronic part and a vibrational part,

$$\psi_{gj}(\mathbf{r}, \mathbf{Q}) = \phi_g(\mathbf{r}, \mathbf{Q})\chi_{gj}(\mathbf{Q}), \quad (31)$$

where  $\mathbf{r}$  describes the electron coordinate, and  $\mathbf{Q}$  the deformation of the molecular geometry. Under the assumption of a transition dipole independent of the molecular deformation, the transition dipoles of the different vibronic transitions factorize as<sup>45</sup>

$$\begin{aligned} \langle \psi_{gj}(\mathbf{r}, \mathbf{Q}) | e\mathbf{r} | \psi_{e0}(\mathbf{r}, \mathbf{Q}) \rangle &= \langle \phi_g(\mathbf{r}, \mathbf{0}) | e\mathbf{r} | \phi_e(\mathbf{r}, \mathbf{0}) \rangle \times \\ &\times \langle \chi_{gj}(\mathbf{Q}) | \chi_{e0}(\mathbf{Q}) \rangle. \end{aligned} \quad (32)$$

Abbreviating the first factor as the transition dipole moment  $\boldsymbol{\mu} = \langle \phi_g(\mathbf{r}, \mathbf{0}) | e\mathbf{r} | \phi_e(\mathbf{r}, \mathbf{0}) \rangle$ , the radiative recombination rate according to eq. (33) can be generalized to

$$k_{\text{S,rad}} = \frac{\boldsymbol{\mu}^2}{3\pi\epsilon_0\hbar^4 c^3} \sum_j E_{e0,gj}^3 n^3(E_{e0,gj}) |\langle \chi_{gj} | \chi_{e0} \rangle|^2, \quad (33)$$

where the sum runs over the vibrational levels in the electronic ground state.<sup>45</sup> Under the additional assumption that the deformation can be approximated by the elongation of an effective internal vibrational mode  $\hbar\omega_{\text{eff}}$ , the different vibronic transitions can be expressed as  $E_{e0,gj} = E_{0e,0g} - j\hbar\omega_{\text{eff}}$ , and the Franck-Condon factors in eq. (33) follow a Poisson progression,

$$|\langle \chi_{gj} | \chi_{e0} \rangle|^2 = e^{-S} \frac{S^j}{j!} \quad (34)$$

where  $S$  is the Huang-Rhys factor of the effective internal vibration, related to the deformation energy  $\lambda_e$  in the relaxed excited geometry as  $\lambda_e = S\hbar\omega_{\text{eff}}$ .<sup>46</sup> A model for the fluorescence lineshape consistent with these assumptions and a normalized lineshape of each vibronic transition reads

$$I_{\text{E}}(E) \propto E^3 n^3(E) \sum_j e^{-S} \frac{S^j}{j!} g(E, E_{e0,gj}, \sigma_j) \quad (35)$$

It is most convenient to express the lineshape of each vibronic sublevel as a normalized Gaussian

$$g(E, E_{0e,gj}, \sigma_j) = \frac{1}{\sqrt{2\pi}\sigma_j} \exp\left(-\frac{(E - E_{0e,gj})^2}{2\sigma_j^2}\right). \quad (36)$$

As discussed elsewhere in more detail, the prefactor  $E^3 n^3(E)$  arises from the density of states of the photons.<sup>32,45</sup> Hence, assuming that the refractive index shows only a weak dependence

on energy, a rescaled fluorescence intensity  $I_E(E)/E^3$  can be fitted to a vibronic progression with weights  $e^{-S}S^j/j!$ , and its energy average

$$\langle E \rangle = E_{e0,g0} - S\hbar\omega_{\text{eff}} \quad (37)$$

corresponds to the vertical energy difference between the potential minimum of the excited electronic configuration and the electronic ground state in the relaxed excited geometry. For these reasons, we transform the observed fluorescence intensity  $I_\lambda(\lambda)$  to  $I_E(E) \propto I_\lambda(\lambda)/E^2$  and fit the rescaled fluorescence intensity  $I_E(E)/E^3$  by a Poisson progression over an effective internal vibration,

$$\frac{I_E(E)}{E^3} \propto \sum_j e^{-S} \frac{S^j}{j!} g(E, E_{e0,gj}, \sigma_j). \quad (38)$$

Fig. 5 reports the emission spectra close to room temperature as a function of wavelength, covering different delay ranges between 2 ns and 2 ms. The emission lineshapes up to a delay of 60  $\mu\text{s}$  remain rather similar, before breaking into two distinct contributions at later delays. For a more quantitative interpretation of the results, all spectra will be transformed into  $I_E(E)/E^3$ , allowing for a lineshape analysis according to eq. (38).

Fig. 6 shows selected lineshapes occurring close to room temperature in different delay ranges. Where applicable, these spectra are fitted over the energy interval 2.0 eV to 3.2 eV with a single Poisson progression according to eq. (38), excluding the low energy region (1.8 to 2.0 eV) where the detector sensitivity depends on energy. Due to eq. (37), even a fit excluding a small region of the observed spectra allows for the definition of a meaningful energy average.

Fig. 7 visualizes lineshape fits for cases where a single Poisson progression can achieve quantitative agreement. At  $T = 300$  K, early delay times (2 ns to 6 ns) result in an energy average  $\langle E \rangle = 2.49$  eV, followed by a red shift towards 2.44 eV in the interval 2  $\mu\text{s}$  to 6  $\mu\text{s}$  before returning to a somewhat higher energy average of 2.45 eV at later times (20  $\mu\text{s}$  to

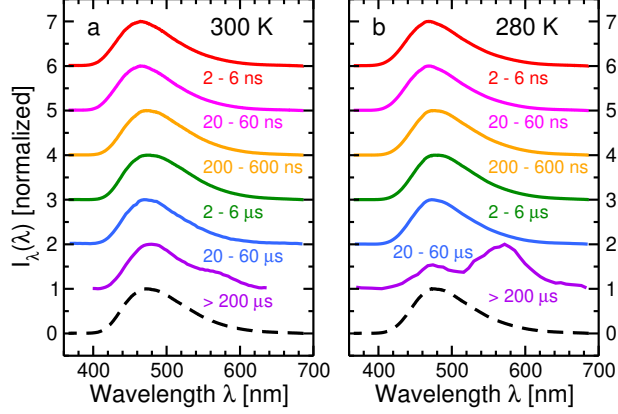


Figure 5: Fluorescence spectra  $I_\lambda(\lambda)$  of a film containing 5 wt.% DMAC-MB embedded in zeonex, integrated over different delay intervals, at temperatures of (a)  $T = 300$  K and (b)  $T = 280$  K. For clarity, each spectrum is normalized to its peak value and shifted vertically, from top to bottom: delay 2 ns to 6 ns (red), 20 ns to 60 ns (magenta), 200 ns to 600 ns (orange), 2  $\mu$ s to 6  $\mu$ s (green), 20  $\mu$ s to 60  $\mu$ s (blue), and time integration from 200  $\mu$ s to 2 ms (purple). At each temperature, the time-integrated spectrum (from 2 ns to 2 ms) is shown as a black dashed line.

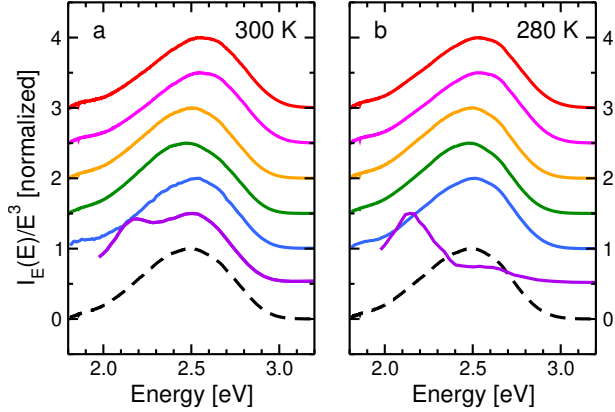


Figure 6: Rescaled fluorescence spectra  $I_E(E)/E^3$  of a film containing 5 wt.% DMAC-MB embedded in zeonex, integrated over different delay intervals, at temperatures of  $T = 300$  K (left) and  $T = 280$  K (right). For clarity, each spectrum is normalized to its peak value and shifted vertically, from top to bottom: delay 2 ns to 6 ns (red), 20 ns to 60 ns (magenta), 200 ns to 600 ns (orange), 2  $\mu$ s to 6  $\mu$ s (green), 20  $\mu$ s to 60  $\mu$ s (blue), and time integration from 200  $\mu$ s to 2 ms (purple). At each temperature, the time-integrated spectrum (from 2 ns to 2 ms) is shown as a black dashed line.

60  $\mu$ s). The spectra at  $T = 280$  K follow a similar trend as a function of delay.

During the two later time intervals mentioned, the measured spectra contain small modulations, indicating a suitable value for an effective internal vibration. On the other hand, at early delays, the fluorescence band shows so little intensity modulation that the effective

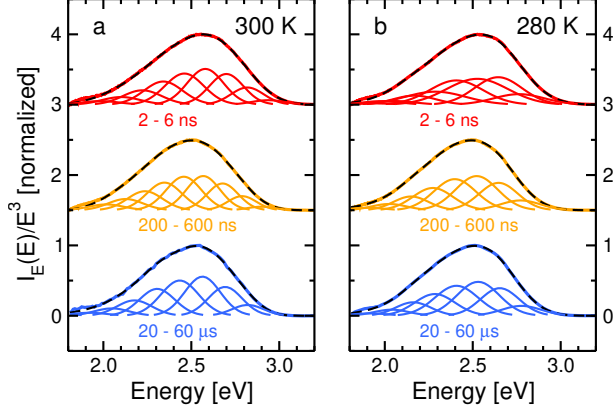


Figure 7: Rescaled fluorescence spectra  $I_E(E)/E^3$  (thick coloured lines) observed at (a)  $T = 300$  K and (b)  $T = 280$  K, with fit according to eq. (38) superimposed (black dashed lines), for cases where an interpretation with a single fluorescence channel is sufficient. All fits were performed over an energy interval extending from 2.0 to 3.2 eV. In each case, the contributions of different vibronic sublevels are shown as coloured lines.

internal mode is merely reduced to a convenient fitting parameter without corresponding to a clear-cut spectroscopic feature. This behaviour is in sharp contrast to compounds revealing a well visible vibronic progression both in absorption and in fluorescence,<sup>45</sup> allowing e.g. to relate the vibronic bands to resonant Raman spectra,<sup>47</sup> vibronic progressions of different internal modes,<sup>48</sup> or to different geometric conformers.<sup>49</sup>

In the delay range from 200  $\mu$ s to 2 ms, the fluorescence bands in Fig. 6 break into two distinct contributions, so that a lineshape analysis requires at least two transitions with their respective deformation patterns. As shown in Fig. 8a, the subband at higher energy occurs at an average energy  $\langle E \rangle$  of  $2.444 \pm 0.002$  eV at  $T = 300$  K and of  $2.46 \pm 0.03$  eV at  $T = 280$  K, and the lower one at an average energy of  $2.13 \pm 0.01$  eV at  $T = 300$  K and of  $2.12 \pm 0.01$  eV at  $T = 280$  K. Hence, within the fitting uncertainties, the position of these bands coincide at both temperatures. At  $T = 200$  K and below, the data contain no red-shifted contribution resembling Fig. 8a.

Fig. 8b shows the average energy  $\langle E \rangle$  of the fluorescence integrated over selected delay intervals. As the low temperature spectra (at  $T = 200$  K and below) show shapes resembling Fig. 7 up to the longest delays investigated, the energy average can be tracked up to the

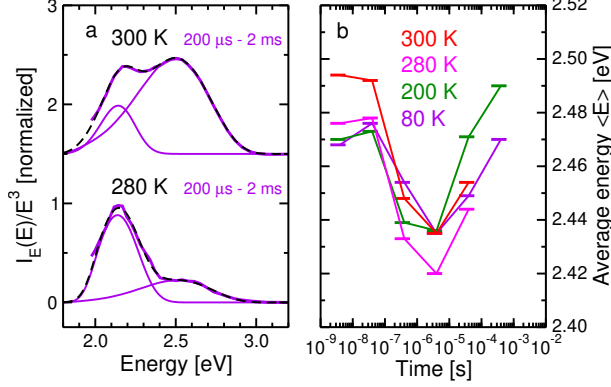


Figure 8: (a) Interpretation of fluorescence lineshapes close to room temperature, for long delays (200  $\mu$ s to 2 ms) requiring a decomposition into two distinct transitions, with the sum of the fitted subbands superimposed (black dashes) on the observed data (thick coloured lines). The fluorescence spectra can be decomposed into similar subbands at both temperatures, but with different relative amplitudes. (b) Average energies  $\langle E \rangle$  in different delay ranges (horizontal bars, integration intervals as in Fig. 6), for selected temperatures:  $T = 300$  K (red),  $T = 280$  K (magenta),  $T = 200$  K (green), and  $T = 80$  K (purple). The straight lines connecting the centers of the different integration intervals (4 ns, 40 ns, 4  $\mu$ s, 40  $\mu$ s, and 400  $\mu$ s) serve as a guide for the eye.

delay window from 200  $\mu$ s to 600  $\mu$ s.

The prompt fluorescence arises from molecules with rather large transition energies, whereas the delayed fluorescence shifts by about 0.05 eV to the red. At very late delays (intervals 20  $\mu$ s to 60  $\mu$ s, and 200  $\mu$ s to 600  $\mu$ s), triplet excitations survive only on emitters which cannot promote up-conversion via TADF, resulting again in somewhat larger transition energies.

## Absorption and photoluminescence excitation

Similar to the fluorescence lineshape, the absorption band corresponding to each electronic transition is influenced by the deformation in the respective relaxed excited geometry. Under assumptions resembling the discussion in Sec. , the imaginary part of the dielectric function can be parametrized as

$$\Im[\varepsilon(E)] = \frac{N}{V} \frac{2\pi\mu^2}{3\varepsilon_0} \sum_j e^{-S} \frac{S^j}{j!} g(E, E_{ej,g0}, \sigma_j) \quad (39)$$

where  $N/V$  is the density of molecules. The vibronic sublevels are now generated by transitions from the lowest vibrational level in the electronic ground state  $S_0$  towards the  $n$ th vibrational level in an excited singlet state,  $E_{ej,g0} = E_{e0,g0} + j\hbar\omega_{\text{eff}}$ , and the shapes  $g(E, E_{ej,g0}, \sigma_j)$  of the different vibronic transitions are parametrized again as normalized Gaussians.

For sufficiently diluted systems, the absorption coefficient  $\alpha(E)$  can be approximated as

$$\alpha(E) = \frac{E}{\hbar cn(E)} \Im[\varepsilon(E)] \quad (40)$$

where  $n(E)$  is the refractive index of the medium, and  $c$  the speed of light.

In a system with weak CT transitions like DMAC-MB, it is more convenient to identify the optical transitions with photoluminescence excitation (PLE) spectroscopy. As PLE is expected to be proportional to the absorption coefficient  $\alpha(E)$  for each transition, but with a different photoluminescence quantum yield for each electronic excitation, we model each PLE band with a shape according to

$$PLE(E) \propto E \sum_j e^{-S} \frac{S^j}{j!} g(E, E_{ej,g0}, \sigma_j) \quad (41)$$

using parameters for the vibronic progression derived from the fluorescence lineshape.

The Poisson fits of the fluorescence spectra discussed in Sec. can be used to interpret the observed PLE spectra reported in Fig. 9. In order to avoid any influence of a blue-shifted fluorescence at early times (2 - 6 ns) and a red-shifted emission band at intermediate delays (2 - 6  $\mu$ s), the fluorescence at  $T = 300$  K integrated over the delay range 20 - 60  $\mu$ s will be taken as a reference for determining the vibronic parameters required in eq. (41). Each PLE band can be assigned to a vertical excitation energy

$$\langle E \rangle = E_{e0,g0} + S\hbar\omega_{\text{eff}}. \quad (42)$$

Table 3 summarizes the excitation energies deduced from the PLE spectra of the three

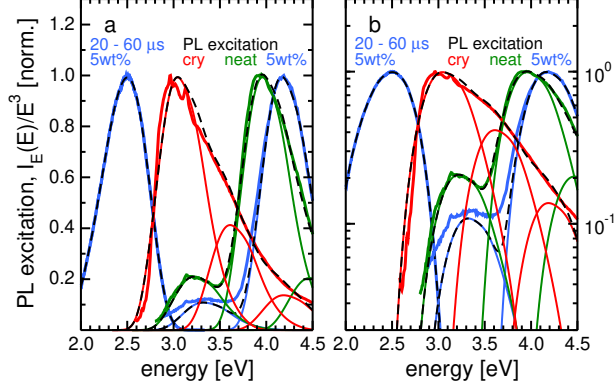


Figure 9: Interpretation of PLE spectra with lineshapes consistent with observed fluorescence, on linear scale (left panel), and on logarithmic scale (right panel). Leftmost curve (blue): Delayed fluorescence at  $T = 300$  K observed on a film with 5wt.% DMAC-MB embedded in zeonex, integrated over delays from 20 to 60  $\mu$ s, with Poisson fit superimposed (black dashed). Rightmost curve (blue): PLE spectra obtained on the same film containing 5wt.% DMAC-MB, interpreted as a sum of two excitation bands (thin blue lines), each with a shape according to eq. (41), using vibronic parameters taken from the fit of the fluorescence lineshape. The sum of both model lineshapes is indicated as a black dashed line. The PLE spectra obtained on a DMAC-MB crystal (red) and on a neat film (green) are decomposed into three subbands, each with a lineshape according to eq. (41).

samples reported in Fig. 9. The diluted sample with 5wt.% DMAC-MB embedded into a zeonex film shows clear evidence for two electronic excitations contributing to the PLE spectra, with average energies of 3.38 eV and 4.23 eV. For the higher of these bands, a lineshape according to eq. (41) quantifies the observed width and asymmetry of the excitation band quite well, whereas the lower band shows a somewhat larger broadening, presumably arising from an influence of the ensemble of different embedding surroundings on a distribution of excitation energies. Interestingly, the neat film reveals no additional broadening, but instead the high energy slope of the upper excitation band indicates the presence of a third but weaker electronic excitation. In the crystalline sample, the relative strength of the two lower bands is reversed, and the overall redshift of all absorption features gives stronger evidence for a third transition above 4 eV.

This analysis demonstrates that the photoluminescence quantum yield of different electronic transitions depends dramatically on the sample under study. For the diluted sample and for the amorphous neat film, the second transition  $S_2 \leftarrow S_0$  dominates the PLE spectra

**Table 3: PLE bands measured while recording the emission at 500 nm (2.48 eV). Vertical transition energies  $\langle E \rangle$  have been derived from the analysis of the observed PLE spectra in Fig. 9, with lineshapes according to eq. (41). The last column refers to transition energies calculated with TD-DFT using an optimally tuned range-separated hybrid functional, compare Sec. for details.**

	5wt.%	neat	crystal	TD-DFT
	eV	eV	eV	eV
$S_1 \leftarrow S_0$	3.38	3.28	3.10	3.42
$S_2 \leftarrow S_0$	4.23	4.02	3.67	4.28
$S_3 \leftarrow S_0$	–	4.53	4.25	4.56; 4.66

by far. In the crystalline sample, on the other hand, the lowest transition  $S_1 \leftarrow S_0$  becomes most prominent, revealing a higher oscillator strength arising for dihedral angles around  $80^\circ$  together with an efficient PL quenching after exciting the higher transitions  $S_2 \leftarrow S_0$  and  $S_3 \leftarrow S_0$ .

The medium surrounding the emitting DMAC-MB molecules exerts a red shift onto the observed absorption resonances, increasing from the diluted sample over the amorphous neat film towards the crystalline sample, compare Fig. 9 and Table 3.

## DFT with range-separated hybrid functionals

### Electronic configurations contributing to observed spectra

The PLE spectra presented in Sec. reveal three prominent absorption bands. The radiative recombination mechanisms include prompt and delayed fluorescence from the minimum of the  $S_1 = {}^1\text{CT}$  potential surface, phosphorescence from a triplet state  $T_1 = {}^3\text{CT}$  giving a quite similar lineshape, and a second red-shifted phosphorescence band resulting from a different triplet minimum  ${}^3\text{A}$  on the acceptor group, becoming most prominent close to room temperature at very late delays. Besides phosphorescence, at late delays, the data give clear evidence for fluorescence from the  $S_1$  state via TTA. Concerning linear up-conversion, TADF via a rISC process was expected by the construction of the donor-acceptor compound, but

this well known phenomenon was supplemented by a second unexpected thermally activated process with a much higher activation energy of about 0.65 eV, assigned to rIC between triplets, with subsequent barrier-less rISC towards the singlet manifold,  ${}^3\text{CT} \rightarrow {}^3\text{A} \rightarrow S_1$ .

All of the above assignments have to be substantiated by a comprehensive modelling of several excited electronic configurations. PLE reveals transitions  $S_1 \leftarrow S_0$ ,  $S_2 \leftarrow S_0$ , and  $S_3 \leftarrow S_0$  in the geometry of the electronic ground state. Assigning these features with DFT calculations requires the development of a range-separated hybrid functional allowing to treat CT states and local donor or acceptor excitations with similar precision. In Sec. , prompt and delayed fluorescence are assigned to radiative recombination from the minimum of the lowest singlet potential surface,  $S_1 \rightarrow S_0$ , and phosphorescence to radiative recombination from two types of relaxed excited triplet potential minima,  ${}^3\text{CT} \rightarrow S_0$  and  ${}^3\text{A} \rightarrow S_0$ . Concerning TTA, symmetry constraints and resonance conditions will help to identify candidates for the process  $T_1 + T_1 \rightarrow S_0 + S_n$  involving an unexpectedly high excited singlet states  $S_n$ , so that excited electronic configurations up to about 5 eV above the electronic ground state have to be tracked.

## Global hybrid B3LYP

As a starting point, we use a ground state geometry optimized with B3LYP,<sup>13</sup> resulting in  $C_s$  symmetry with the benzoate confined to the mirror plane. The frontier orbitals consist of a  $\pi$  HOMO on the DMAC donor and a  $\pi^*$  LUMO on the MB acceptor. Hence, for determining the potential minimum of the lowest CT triplet  $T_1$ , the most simple procedure relies on a minimization of the total energy in the respective spin configuration. The global  $T_1$  minimum occurs in a twisted geometry with a dihedral angle of  $63.2^\circ$  around the donor-acceptor connection. Total energies and lowest CT transitions obtained in the  $S_0$  ( $C_s$ ) ground state geometry and in the optimized  $T_1$  ( $C_s$ ) and twisted  $T_1$  ( $C_1$ ) geometries are summarized in Table 4. The singlet-triplet splitting remains quite small in optimized ground and excited state geometries conserving  $C_s$  mirror symmetry, but it increases strongly in

twisted geometries with a dihedral angle differing from  $90^\circ$ .

The calculated CT transition energy  $S_1 \leftarrow S_0$  of 2.69 eV in the ground state geometry remains about 0.7 eV below the lowest observed PLE resonance for DMAC-MB embedded into a zeonex film, compare Fig. 9 and Table 3. Similarly, the calculated  $S_1 \leftarrow S_0$  transition energies in Table 4 obtained in different relaxed excited geometries are smaller than the average energies of the scaled fluorescence intensities  $I_E(E)/E^3$  displayed in Fig. 6. These deviations corroborate once more that CT transition energies are severely underestimated when applying TD-DFT with the global hybrid B3LYP, including questionable estimates for the respective Stokes shift.

Concerning higher transitions obtained with TD-DFT in the ground state geometry, a second weak CT transition  $S_2 \leftarrow S_0$  from HOMO to LUMO+1 occurs at 3.56 eV. The lowest stronger transitions  $S_3 \leftarrow S_0$  and  $S_4 \leftarrow S_0$  arise at 4.19 eV and 4.28 eV, respectively, promoting a DMAC HOMO electron to one of the two lowest virtual  $\pi^*$  orbitals on the same donor group. These two calculated transition energies correspond roughly to the strong PLE band reported in Fig. 9 and could possibly serve as a realistic assignment for a strongly absorbing transition on the donor.

As demonstrated for various polyaromatic compounds, TD-DFT in B3LYP is likely to overestimate singlet-triplet splittings with respect to spectroscopic evidence, but this systematic deviation can be reduced in the Tamm-Dancoff approximation (TDA). Table 5 reports the respective TDA transition energies in the optimized ground state geometry. From a comparison between TD-DFT in Table 4 and TDA in 5, it turns out that the lowest CT state remains essentially unaffected, whereas for higher transitions with large orbital overlap, TDA gives a somewhat reduced singlet-triplet splitting, as expected from previous work.<sup>50</sup> Hence, TDA might give slight improvements for higher transitions, but as far as the lowest CT state of our model compound is concerned, both approaches perform similarly.

Our B3LYP TD-DFT calculations demonstrate once again that transitions with large oscillator strength like the two lowest donor excitations  $S_3 \leftarrow S_0$  and  $S_4 \leftarrow S_0$  are reasonably

Table 4: Total energy  $E_{\text{tot}}$  of DMAC-MB in optimized geometries for different electronic configurations, transition energies and oscillator strength for excitation in ground state geometry, Kohn-Sham energies of frontier orbitals, and calculated values of ionization potential (IP) and electron affinity (EA). All values have been obtained at the B3LYP/6-31G(d) level, and transition energies with TD-DFT using the same global hybrid.

geometry	$S_0 (C_s)$		$T_1 (C_s)$	$T_1 (C_1)$
	eV	$f_{\text{osc}}$	eV	eV
$E_{\text{tot}}$	0		2.96	2.88
$S_1 \leftarrow S_0$	2.69	$< 5 \times 10^{-5}$	2.11	2.31
$S_2 \leftarrow S_0$	3.56	0.0004		
$S_3 \leftarrow S_0$	4.19	0.022		
$S_4 \leftarrow S_0$	4.28	0.105		
$T_1 \leftarrow S_0$	2.67		2.10	2.08
$T_2 \leftarrow S_0$	3.22			
$T_3 \leftarrow S_0$	3.49			
$T_4 \leftarrow S_0$	3.53			
$\Delta_{\text{ST}}$	0.018		0.017	0.22
$\varepsilon_{\text{HOMO}}$	-4.88		-4.77	-4.88
$\varepsilon_{\text{LUMO}}$	-1.46		-1.92	-1.86
IP	6.31			
EA	-0.22			

Table 5: Transition energies and oscillator strengths for excitation in ground state geometry, calculated with TDA at the B3LYP/6-31G(d) level, and transition energies with TDA in two relaxed triplet geometries.

geometry	$S_0 (C_s)$		$T_1 (C_s)$	$T_1 (C_1)$
	eV	$f_{\text{osc}}$	eV	eV
$S_1 \leftarrow S_0$	2.68	$< 5 \times 10^{-5}$	2.12	2.34
$S_2 \leftarrow S_0$	3.56	0.0002		
$S_3 \leftarrow S_0$	4.26	0.026		
$S_4 \leftarrow S_0$	4.33	0.013		
$T_1 \leftarrow S_0$	2.66		2.10	2.13
$T_2 \leftarrow S_0$	3.41			
$T_3 \leftarrow S_0$	3.56			
$T_4 \leftarrow S_0$	3.62			
$\Delta_{\text{ST}}$	0.017		0.017	0.22

well described, whereas CT transition energies are severely underestimated.

Due to the equivalent results of TD-DFT and TDA for the lowest CT state of our model system obtained with B3LYP, in the following calculations of transition energies and optimized triplet geometries with an optimally tuned range-separated hybrid functional, we will use TD-DFT throughout.

## Problems of DFT when applied to CT states

Koopmans' theorem in Hartree-Fock guarantees that ionization potential IP and binding energy of HOMO orbital  $\varepsilon_{\text{HOMO}}$  correspond to each other as  $\text{IP} = -\varepsilon_{\text{HOMO}}$ . In sharp contrast, density functional theory (DFT) with standard GGA functionals deviates from this behaviour. This systematic shortcoming arises from asymptotics of the exchange-correlation functional differing from the correct Coulomb potential, and together with the erroneous continuity of the Kohn-Sham potential as a function of electron number, this results in a severe underestimate of the HOMO-LUMO gap  $\varepsilon_{\text{LUMO}} - \varepsilon_{\text{HOMO}}$  with respect to the difference  $\text{IP} - \text{EA}$  between ionization potential and electron affinity, known as the gap error.<sup>51,52</sup>

A somewhat improved asymptotic behaviour of the exchange-correlation potential can be recovered with global hybrid functionals involving a fraction of non-local exchange like B3LYP,<sup>13</sup> but such a procedure eliminates only a part of the gap error.

In our B3LYP ground state calculations summarized in Table 4, the Kohn-Sham orbital energies correspond to  $\varepsilon_{\text{HOMO}} = -4.88$  eV and  $\varepsilon_{\text{LUMO}} = -1.46$  eV, showing a quite poor correspondence with an ionization potential of  $\text{IP} = 6.31$  eV and an electron affinity  $\text{EA} = -0.22$  eV calculated from the difference of the total energies of neutral and ionized electronic configurations. The negative EA might indicate that in vacuum, the DMAC-MB molecule remains still too small to bind an additional electron. The fundamental gap between quasi-electron excitation and quasi-hole excitation corresponds to  $\text{IP} - \text{EA} = 6.53$  eV, poorly reproduced by the difference of Kohn-Sham orbital energies  $\varepsilon_{\text{LUMO}} - \varepsilon_{\text{HOMO}} = 3.42$  eV.

## Range-separated hybrid functionals

A partition of the Coulomb interaction into a long-range and a short-range part can be applied to an improved definition of a range-separated hybrid functional, where the short-range exchange is modelled as a local potential in the spirit of DFT, but the long-range part is treated as non-local Fock exchange.<sup>19,20</sup> Such schemes eliminate most of the notorious deviations of time-dependent DFT (TD-DFT) calculations where CT excitations would be misplaced with respect to local excitations.<sup>19,22</sup>

The range separation of the Coulomb interaction can be achieved by a smooth interpolation function via an exponential<sup>20</sup> or an error function  $\text{erf}(\gamma r)$ <sup>19,21</sup>

$$\frac{1}{r} = \frac{\alpha + \beta \text{erf}(\gamma r)}{r} + \frac{1 - \alpha - \beta \text{erf}(\gamma r)}{r}, \quad (43)$$

where  $\alpha$ ,  $\beta$  and  $\gamma$  are model parameters. For a finite value of the range separation parameter  $\gamma$ , the first term behaves asymptotically as  $(\alpha + \beta)/r$  for large inter-electronic distance  $r$ . The respective part of the Coulomb interaction will be treated with non-local exchange like in Hartree-Fock theory. With the additional constraint  $\alpha + \beta = 1$ , this approach guarantees the correct asymptotic behaviour of the Coulomb interaction at large distance, and the second term becomes short-range, so that it can be treated with an exchange-correlation functional. In the limit  $\gamma r \rightarrow 0$ , the expression in eq. (44) simplifies to

$$\frac{1}{r} = \frac{\alpha}{r} + \frac{1 - \alpha}{r} \quad (44)$$

so that the underlying hybrid functional with a fraction  $\alpha$  of non-local exchange is recovered, where the complement  $(1 - \alpha)$  is handled with a density functional accounting for local exchange and correlation.

From various comparisons of the performance of global hybrids, it is well established that a range  $0.2 \leq \alpha \leq 0.3$  gives particularly reliable molecular geometries and vibrational

modes.<sup>48,53,54</sup> Even though the energies of the frontier orbitals do not correspond to ionization potential and electron affinity, TD-DFT with such functionals gives rather reliable transition energies, with the exception of CT states.<sup>12,55–57</sup> For these reasons, we use the hybrid B3LYP with  $\alpha = 0.2$  as a reference for a range-separated hybrid, abbreviated in the following as LC-B3LYP.

## Determination of range-separation parameter via Koopmans’ theorem

As discussed elsewhere in more detail, range-separated hybrid functionals achieve quite high predictive power for a specific molecule with  $N$  electrons if a generalization of Koopmans’ theorem is applied to the most suitable choice of the range-separation parameter  $\gamma$ :<sup>22,58–60</sup>

$$-\varepsilon_{\text{HOMO}}(N, \gamma) \stackrel{!}{=} E_g(N-1, \gamma) - E_g(N, \gamma) = \text{IP}(N, \gamma), \quad (45)$$

where  $\varepsilon_{\text{HOMO}}$  is the Kohn-Sham energy of the HOMO, and  $E_g(N-1, \gamma)$  and  $E_g(N, \gamma)$  are the ground state energies for the cationic and neutral system, respectively, so that their difference corresponds to the ionization potential of the  $N$  electron system. Even though Koopmans’ theorem in its original form does not address energies of virtual states, the Kohn-Sham energy of the LUMO can be related to the ionization potential of the negatively charged ( $N+1$ ) electron system by enforcing

$$-\varepsilon_{\text{LUMO}}(N, \gamma) \stackrel{!}{=} E_g(N, \gamma) - E_g(N+1, \gamma) = \text{EA}(N, \gamma), \quad (46)$$

corresponding to the electron affinity of the  $N$  electron molecule. Obviously, both constraints eqs. (45,46) cannot be fulfilled simultaneously with the best choice of a single parameter  $\gamma$ , but a compromise between them can be found by minimizing an expression involving both

targets, e.g.<sup>60</sup>

$$\begin{aligned} \delta^2(\gamma) &= [\varepsilon_{\text{HOMO}}(N, \gamma) + \text{IP}(N, \gamma)]^2 \\ &+ [\varepsilon_{\text{LUMO}}(N, \gamma) + \text{EA}(N, \gamma)]^2. \end{aligned} \tag{47}$$

In contrast to the CAM-B3LYP scheme, the Coulomb asymptotics of our approach corresponds to an unscreened Coulomb interaction, and the range separation parameter  $\gamma$  is adjusted to the specific system under study, not to a global training set of rather small molecules.<sup>21</sup>

## Application to DMAC-MB

In the following, we apply the above scheme to our model TADF emitter DMAC-MB presented in Sec. . All calculations have been performed with the NWChem program package.<sup>61</sup>

For a 6-31G\* variational basis set and the range-separated hybrid LC-B3LYP, the choice  $\alpha = 0.2$  from B3LYP,  $\beta = 1 - \alpha = 0.8$ , and  $\gamma = 0.0168/a_{\text{B}} = 0.317/\text{\AA}$ , we find a minimum of  $\delta(\gamma) = 0.13$  eV, corresponding to a deviation between  $-\varepsilon_{\text{HOMO}}$  and IP of 0.09 eV and between  $-\varepsilon_{\text{LUMO}}$  and EA of 0.09 eV, compare Fig. 10a. The fundamental gap between charged quasiparticle excitations is reproduced even more precisely, with  $\text{IP} - \text{EA} = 6.70$  eV and  $\varepsilon_{\text{LUMO}} - \varepsilon_{\text{HOMO}} = 6.71$  eV.

Optimizing the B3LYP ground state geometry again with LC-B3LYP and the above choice of parameters  $\alpha$ ,  $\beta$ , and  $\gamma$ , we find only a minor change of the total energy of  $\Delta E = -0.05$  eV. This demonstrates that the long-range correction of the global hybrid B3LYP has quite little influence on the bond geometries, which are merely determined by short-range Hartree potential, exchange and correlation.

Fig. 10 reports deviations  $\delta(\gamma)$  obtained after optimizing the molecular geometry within the point group  $C_s$  for each set of parameters  $\alpha = 0.2$ ,  $\beta = 0.8$ , and  $\gamma$ , in the three electronic configurations  $S_0(a')$ ,  ${}^3\text{CT}(a'')$  and  ${}^3\text{A}(a')$ . The results demonstrate that the best

range separation parameter  $\gamma$  is hardly affected by deformations occurring at the potential minima of excited triplet configurations, with changes of up to  $-0.0011$ , or  $-0.7\%$ . Hence, for the following calculation of various deformation patterns and excited electronic configurations, we will use the parameter  $\gamma = 0.168/a_B$  determined in the geometry of the electronic ground state  $S_0$ . The range separation parameter  $\gamma$  assumes a value resembling similar approaches,<sup>24,26,31</sup> and with respect to CAM-B3LYP trained on smaller molecules, it remains significantly smaller, corresponding to a larger distance  $1/\gamma$  governing the switching of the error function in eq. (44) to exact non-local exchange.

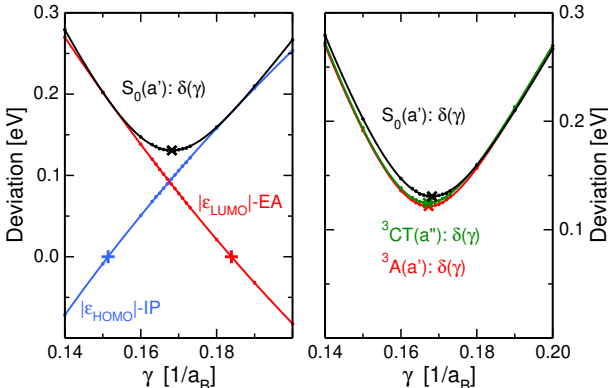


Figure 10: Determination of range separation parameter  $\gamma$  for optimized geometries in different electronic configurations respecting  $C_s$  mirror symmetry. (a) for  $S_0(a')$  configuration, (b) comparison of optimized geometries in the configurations  $S_0(a')$ ,  ${}^3CT(a'')$ , and  ${}^3A(a')$ , evaluated in the electronic ground state  $S_0$ . For each data point (dots), the geometry has been optimized in the respective electronic configuration. Colored lines are based on cubic polynomials fitted to  $|\epsilon_{\text{HOMO}}| - IP$  and  $|\epsilon_{\text{LUMO}}| - EA$ . For the latter two, zero crossings are marked (+), together with the minimum of  $\delta(\gamma)$  (x).

The orbitals contributing most prominently to the electronic transitions of interest are depicted in Fig. 11. All of them are localized preferentially on either donor and acceptor, so that electronic transitions can easily be assigned to local donor excitations, local acceptor excitations, or CT transitions.

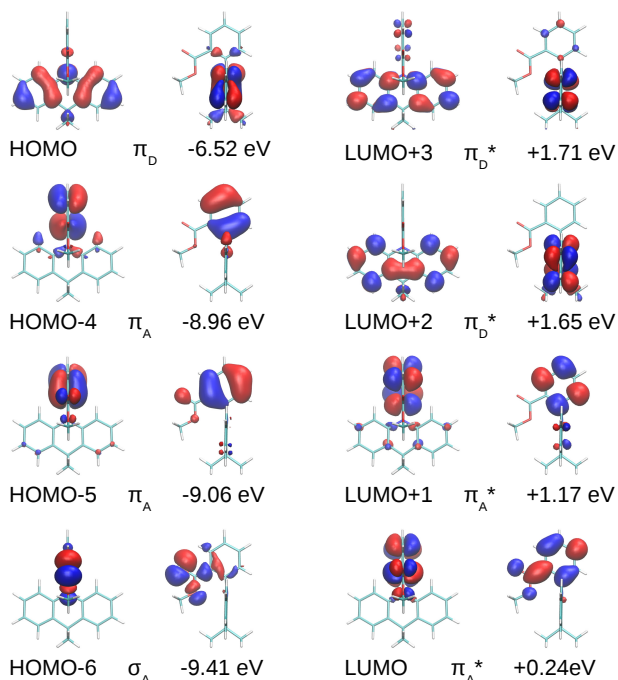


Figure 11: Selected Kohn-Sham orbitals of DMAC-MB, calculated with the optimally tuned range-separated hybrid functional LC-B3LYP. Left: occupied orbitals, right: virtual orbitals.

## Assignment of absorption bands

In Sec. , the optical excitations of DMAC-MB were mapped via PLE spectra. The lowest calculated CT excitation  $S_1 \leftarrow S_0$  in Table 6 at 3.42 eV compares favourably with the lowest PLE resonance occurring at 3.38 eV in the diluted sample (5wt.%), and at somewhat lower energies in the amorphous film and in the crystalline sample, compare Table 3. The second PLE band can be assigned to the second CT excitation  $S_2 \leftarrow S_0$  at 4.28 eV, achieving again an astounding agreement with the PLE resonance observed at 4.23 eV in the diluted sample. The calculated oscillator strengths of these two CT excitations give a ratio of 9.7, in reasonable agreement with the observations, compare Fig. 9.

The third excitation band assigned to the PLE spectra in Fig. 9 corresponds either to the still rather weak donor excitation  $S_3 \leftarrow S_0$ , or to one of the much stronger donor excitations  $S_4 \leftarrow S_0$  and  $S_5 \leftarrow S_0$ , presumably somewhat redshifted due to the interaction between the emitter and the polarizable medium. The lowest acceptor excitations  $S_6 \leftarrow S_0$  and  $S_7 \leftarrow S_0$  exceed 5 eV, in each case with rather small oscillator strength.

**Table 6: Electronic excitations calculated with TD-DFT using the optimally tuned long-range corrected hybrid LC-B3LYP: transition energies, oscillator strength, assignment involving the representation in the  $C_s$  point group, and dominating contribution in terms of transitions between ground state Kohn-Sham orbitals, compare Fig. 11 for a visualization.**

	$E$ eV	$f_{osc}$ 1	assignment		
$S_1 \leftarrow S_0$	3.42	0.00043	CT	$a''$	94% HOMO→LUMO
$S_2 \leftarrow S_0$	4.28	0.00417	CT	$a''$	90% HOMO→LUMO+1
$S_3 \leftarrow S_0$	4.56	0.0273	D	$a'$	89% HOMO→LUMO+2
$S_4 \leftarrow S_0$	4.66	0.1586	D	$a''$	92% HOMO→LUMO+3
$S_5 \leftarrow S_0$	4.96	0.1299	D	$a''$	77% HOMO→LUMO+4
$S_6 \leftarrow S_0$	5.04	0.00001	A	$a''$	90% HOMO-6→LUMO
$S_7 \leftarrow S_0$	5.14	0.0354	A	$a'$	67% HOMO-4→LUMO
$T_1 \leftarrow S_0$	3.33	–	D	$a''$	57% HOMO→LUMO+3
$T_2 \leftarrow S_0$	3.40	–	CT	$a''$	87% HOMO→LUMO
$T_3 \leftarrow S_0$	3.52	–	A	$a'$	55% HOMO-5→LUMO

### Geometry optimization in different electronic configurations

The geometries in different excited triplet configurations are optimized with TD-DFT, resulting in three distinct mirror-symmetric ( $C_s$ ) geometries for  ${}^3\text{CT}(a'')$ ,  ${}^3\text{D}(a'')$ , and  ${}^3\text{A}(a')$ . Moreover, starting from the lowest among these three triplet minima,  ${}^3\text{CT}(a'')$ , it turns out that a reduced dihedral angle between donor and acceptor gives an even lower triplet minimum, called  ${}^3\text{CT}(C_1)$  in the following.

Fig. 12 visualizes the deformations in different  $C_s$  symmetric relaxed triplet geometries. As expected, the optimized geometries of  ${}^3\text{A}$  and  ${}^3\text{D}$  with local triplet excitations carry mainly deformations on either acceptor or donor, whereas in  ${}^3\text{CT}$ , the hole in the HOMO deforms the DMAC donor, and the electron in the LUMO the MB acceptor. In addition, around the nitrogen atom, deviations of the bond geometry from planarity depend on the respective electronic configuration.

The distorted geometry of the global triplet minimum is shown in Fig. 13, revealing a reduced average dihedral angle of  $57.4^\circ$  between donor and acceptor ( $50.1^\circ$  towards carboxylate,  $64.8^\circ$  towards other part of phenyl), together with further out-of-plane distortions of

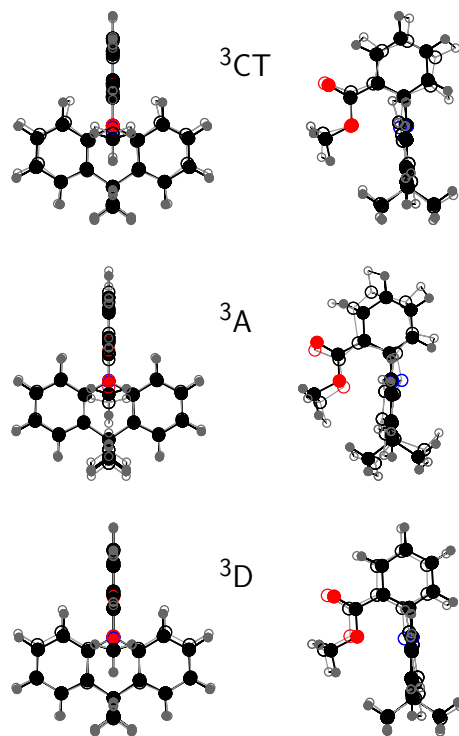


Figure 12: Deformations of DMAC-MB in different optimized  $C_s$  symmetric triplet geometries, as annotated. The deformations with respect to the  $C_s$  ground state geometry multiplied by a factor of 5. The deformed geometries (open circles, grey bonds) are superimposed to the ground state geometry (filled circles, black bonds).

the methoxy group.

A generalization of range-separated hybrid functionals to embedding media with a dielectric constant  $\varepsilon > 1$  can be obtained by choosing  $\beta$  according to  $\alpha + \beta = 1/\varepsilon$ , and this approach reproduces the essential trends for ionization potential and electron affinity of molecules embedded into a polarizable medium or into a molecular crystal.<sup>62</sup>

In a recent study of donor-acceptor compounds consisting of a DMAC donor and different isomers of benzonitrile as the acceptor, it was demonstrated that such a scheme reproduces the observed red-shift of intramolecular CT transitions as a function of increasing dielectric constant as well.<sup>63</sup> Interestingly, this embedding scheme stabilizes  $C_s$  symmetric CT triplet minima against CT triplets in distorted geometries with dihedral angle between donor and acceptor differing from  $90^\circ$ . Moreover, a comparison of the calculated B3LYP transition energies in Table 4 obtained with TD-DFT and the respective values in Table 5 calculated

with TDA give further evidence that a possible stabilization of triplet minima in distorted geometries may be reduced. Therefore, the additional stabilization of the  $^3\text{CT}$  triplet for reduced dihedral angle we obtain with TD-DFT using the optimally tuned range separated functional LC-B3LYP might quite well be an artifact arising from the lack of an embedding medium in our numerical approach.

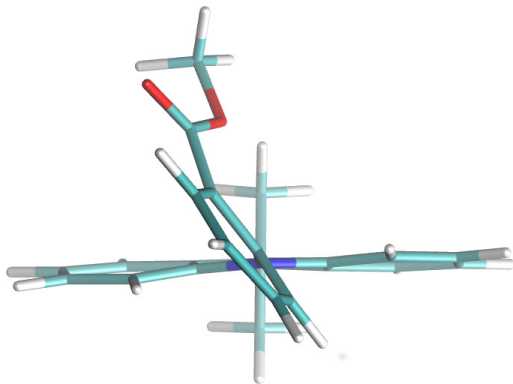


Figure 13: Optimized geometry of DMAC-MB in the  $C_1$  symmetric global  $^3\text{CT}$  minimum.

## Excited potential surfaces

Fig. 14 interpolates the singlet potential surfaces  $S_0$  to  $S_{10}$  and the triplet potential surfaces  $T_1$  to  $T_{10}$  between the optimized reference geometries. As in other TADF systems,<sup>64</sup> triplet excitations are rather densely spaced, so that the tenth triplet  $T_{10}$  is roughly in resonance with the third excited singlet  $S_3$ . Within the constraint of  $C_s$  mirror symmetry, the lowest CT excitations  $^1\text{CT}$  and  $^3\text{CT}$  remain close to parallel, with a splitting varying between  $\Delta_{\text{ST}} = 23$  meV in the  $S_0$  ground state geometry towards a slightly lower value of  $\Delta_{\text{ST}} = 21$  meV in the optimized  $^3\text{CT}$  geometry.

When comparing the calculated potential minima of the three types of triplet minima occurring in different mirror-symmetric geometries, it turns out that they are nearly degenerate: 3.06 eV for  $^3\text{CT}$ , 3.11 eV for  $^3\text{A}$ , and 3.14 eV for  $^3\text{D}$ . However, due to the very different deformation energies on the ground state potential, this corresponds to quite different calculated transition energies for recombination: 2.72 eV for  $^3\text{CT}$ , 2.54 eV for  $^3\text{A}$ , and 2.92 eV

for  ${}^3D$ . At reduced dihedral angle, the global triplet minimum occurs for the optimized  ${}^3CT$  geometry at an energy of 2.85 eV, corresponding to a transition energy of 2.26 eV towards the electronic ground state.

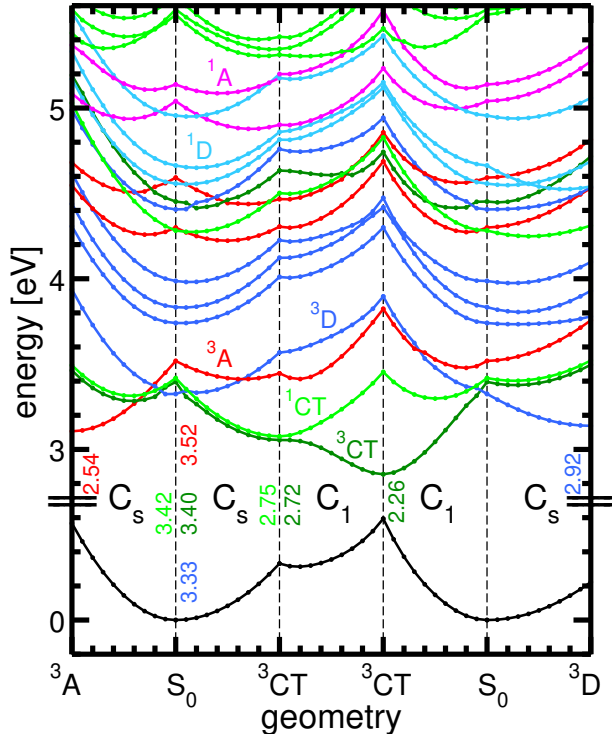


Figure 14: Singlet potential surfaces  $S_1$  to  $S_{10}$  (light colours), triplet potential surfaces  $T_1$  to  $T_{10}$  (dark colours), together with ground state  $S_0$  potential surface (black), for deformations between ground state geometry  $S_0$  and different optimized triplet geometries. Each type of excitation is depicted with a different colour for the respective potential surfaces:  ${}^1CT$  (light green),  ${}^3CT$  (dark green),  ${}^1A$  (magenta),  ${}^3A$  (red),  ${}^1D$  (light blue),  ${}^3D$  (dark blue). Deformations conserving  $C_s$  mirror symmetry are marked, together with the symmetry lowering ( $C_1$ ) towards smaller dihedral angles. Each deformation is scaled in steps of 10%, and for deformations deviating from mirror symmetry, modified dihedral angles (between donor and acceptor, and within benzoate group) and planar deformations of subgroups are scaled separately. Transition energies starting from different potential minima are marked in the respective colour (in eV).

Before attempting to assign the observed fluorescence spectra, we have to answer the question whether the triplet minima  ${}^3A$  and  ${}^3D$  in mirror-symmetric geometries are stable, or whether they can convert in a barrierless fashion towards the global symmetry-broken  ${}^3CT$  minimum. Fig. 15 reveals that each minimum is stable within  $C_s$  symmetry, and  ${}^3D$  remains even stable for geometries with reduced dihedral angle approaching the symmetry-

broken geometry of the absolute triplet minimum  ${}^3\text{CT}$ . For reduced dihedral angle, the  ${}^3\text{A}$  minimum acquires more and more CT character, so that it can convert to the overall  ${}^3\text{CT}$  minimum without potential barrier. As mentioned already in Sec. , generalizations of the optimally tuned hybrid LC-B3LYP to a polarizable medium with  $\varepsilon > 1$  or to transition energies calculated with TDA may quite well reduce this stabilization of the  ${}^3\text{CT}$  potential minimum in distorted geometries, so that  $C_s$  symmetric  ${}^3\text{CT}(a'')$  and  ${}^3\text{A}(a')$  potential minima would become globally stable.

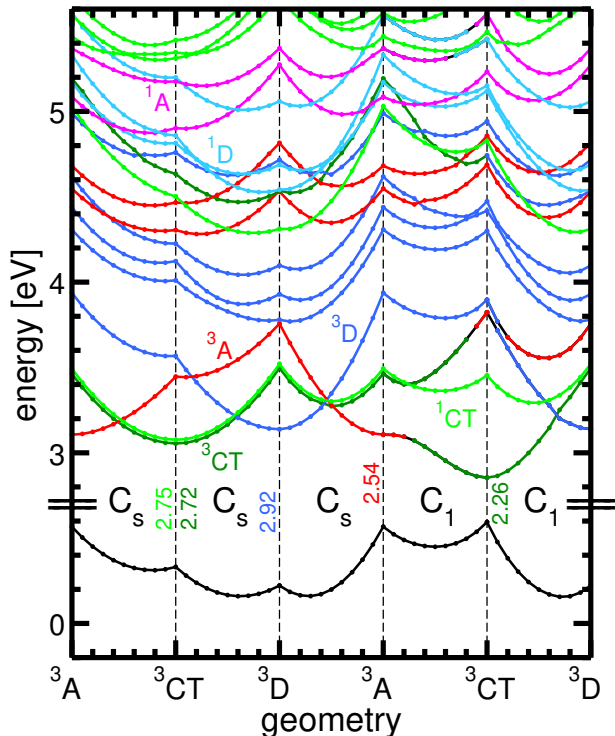


Figure 15: Singlet and triplet potential surfaces (coloured) together with ground state  $S_0$  potential surface (black), for deformations between different optimized triplet geometries:  ${}^1\text{CT}$  (light green),  ${}^3\text{CT}$  (dark green),  ${}^1\text{A}$  (magenta),  ${}^3\text{A}$  (red),  ${}^1\text{D}$  (light blue),  ${}^3\text{D}$  (dark blue). For each potential surface, the colour corresponds to the dominating contribution. Concerning the lowest three triplets, for the non-symmetric ( $C_1$ ) geometries, the dominating type of triplet excitation changes along the deformation pathway, as indicated by the colour change.

# Assignment of fluorescence bands

## Fluorescence from $S_1$ minimum

From the fluorescence lineshapes reported in Fig. 6, it became clear that up to a delay of about 60  $\mu\text{s}$ , the energy average of  $I_E(E)/E^3$  corresponding to the vertical transition energy from the excited state potential minimum down to the electronic ground state evolved in a rather narrow energy window shown in Fig. 8b. Only at high temperatures and later times, the fluorescence breaks into two subbands, where the higher one still remains close to the shape observed earlier. Hence, fluorescence arises from essentially the same type of relaxed geometry over a delay range up to about 60  $\mu\text{s}$ , corresponding most likely to the relaxed  $S_1$  potential minimum, modelled as the mirror-symmetric  $^3\text{CT}$  geometry in Figs. 14 and 15. The presence of a strong TADF contribution up to a delay of about 100  $\mu\text{s}$  underpins that triplets with low activation energy have to survive up to this time scale, and the Arrhenius plot in Fig. 4 sets the respective energy scale for the activation energy: about 43 meV for the stronger and faster of the two TADF channels observed. Such low activation energies from a triplet state to a neighbouring singlet can only occur in the surroundings of this mirror-symmetric relaxed configuration, as depicted in Fig. 14. The observed activation energy slightly above the calculated singlet-triplet splitting  $\Delta_{\text{ST}} = 21$  meV in this relaxed geometry arises from small distortions of the dihedral angle away from orthogonal orientation between donor and acceptor group. A substantial part of the triplet population seems to survive in geometries where the dihedral angle cannot evolve freely towards a distorted  $^3\text{CT}$  triplet minimum, giving a further indication that the  $C_s$  symmetric  $^3\text{CT}$  minimum is globally stable.

With respect to the excellent correspondence between observed PLE bands in Fig 9 and Table 3 and the calculated transitions in Table 6, the agreement between observed fluorescence bands centered between 2.42 eV and 2.49 eV (see Fig. 8b) and the calculated  $S_1 \rightarrow S_0$  fluorescence transition at 2.75 eV remains much poorer. Taking 2.46 eV as the average observed fluorescence transition energy reported in Fig. 8b, the measured Stokes

shift with respect to the lowest PLE resonance in Table 3 amounts to 0.92 eV, whereas the calculated Stokes shift deduced from TD-DFT with the optimally tuned range-separated hybrid depicted in Fig. 14 corresponds to only 0.67 eV, or about 73% of the observed value. It is not uncommon that excited state deformations relying on TD-DFT fall short of deformations derived directly from spectroscopic observables or from calculations with constraints on orbital occupations or spin configuration, compare e.g. B3LYP calculations on perylene pigments.<sup>65</sup> The detailed comparison between measured and calculated Stokes shift of the most prominent contribution to fluorescence from DMAC-MB indicates that the optimally tuned long-range corrected variant of B3LYP applied in the present work does not cure this deficiency. Calculated and measured Stokes shift would be reconciled if the deformation energy in the  $S_1$  potential minimum would increase from the calculated value of 0.33 eV reported in Fig. 14 to 0.48 eV.

## Radiative recombination rate

At the  $^1\text{CT}$  potential minimum, the oscillator strength of the transition  $S_1 \leftarrow S_0$  is only 0.00008, so that the radiative lifetime for fluorescence  $S_1 \rightarrow S_0$  would be as slow as 20  $\mu\text{s}$ , about 50 times longer than observed. However, thermal modulations of the dihedral angle promote much larger oscillator strengths via Herzberg-Teller coupling to other electronic configurations. In a scan of the dihedral angle with rigid D and A groups, a Boltzmann distribution in the somewhat non-parabolic potential minimum provides an average thermal energy of  $0.46 k_{\text{B}}T$ , slightly below the value of  $k_{\text{B}}T/2$  expected for a parabolic potential. The average of the radiative rate over such a Boltzmann distribution at  $T = 300 \text{ K}$  gives  $\langle k_{\text{S,rad}} \rangle = 1.04 \times 10^6 \text{ s}^{-1}$ , compatible with an average angular distortion  $\Delta\Phi = \langle (\Phi - 90^\circ)^2 \rangle^{1/2}$  of  $\Delta\Phi = 5.7^\circ$  away from orthogonal orientation of DMAC donor and MB acceptor. Assuming that the embedding into the rather rigid zeonex matrix promotes further angular distortions, a broader distribution resulting in  $\Delta\Phi = 7.1^\circ$  would provide sufficient dipolar coupling strength to increase the average radiative recombination rate to a value of  $\langle k_{\text{S,rad}} \rangle = 1.6 \times 10^6 \text{ s}^{-1}$ , as

observed. Such a broader distribution would require an average energy of about  $0.72 k_{\text{B}}T$ , or only  $0.26 k_{\text{B}}T$  above the Boltzmann average calculated for the free molecule.

## Activation barrier for reverse intersystem crossing

The increased singlet-triplet splitting  $\Delta_{\text{ST}}$  at dihedral angles differing from the orthogonal D-A arrangement can be used to cross-check the above arguments. A Boltzmann distribution with an average angular distortion of  $\Delta\Phi = 5.7^\circ$  would result in  $\langle\Delta_{\text{ST}}\rangle = 36$  meV, increasing towards  $\langle\Delta_{\text{ST}}\rangle = 45$  meV for  $\Delta\Phi = 7.1^\circ$ . Both values are in the correct range of activation energies determined from the Arrhenius fits in Fig. 4.

We expect that ensemble averages over ISC or rISC rates can be quantified with range-separated hybrid functionals in a similar way as the average radiative recombination rate.<sup>29</sup> This would require to calculate the dominating spin-orbit matrix elements<sup>17,66,67</sup> with an optimally tuned range-separated hybrid functional like the one discussed in the present work, to track these matrix elements along symmetry breaking distortions, and to calculate averages over geometry distributions. For the system under study, this would require a DFT approach giving a torsional potential stabilizing an orthogonal angle between donor and acceptor, e.g. by generalizing the present approach to embedding schemes accounting for the polarizable medium.<sup>62,63</sup> Hence, we do not attempt to apply the optimally tuned range separated hybrid LC-B3LYP to average rates of ISC or rISC, and instead, we leave such investigations to future work.

## Reverse internal conversion between triplets

When comparing the quite high activation energy around 0.61 eV to 0.69 eV derived from the fit in Fig. 4b with the excited potential surfaces in Fig. 15 above the mirror-symmetric  $^3\text{CT}$  minimum, it turns out that this activation energy is roughly resonant with the calculated transition energy  $T_3(^3\text{A}(a')) \leftarrow T_1(^3\text{CT}(a''))$  of 0.51 eV, ending on an excited acceptor triplet. When accounting for a larger deformation energy of 0.48 eV at the  $^3\text{CT}(a'')$  potential

minimum derived from the observed Stokes shift mentioned in Sec. , this potential minimum would be lowered by 0.15 eV, bringing the expected barrier  $T_3(^3A(a')) \leftarrow T_1(^3CT(a''))$  even closer to the observed value around 0.65 eV.

Hence, the increase of the rate of delayed fluorescence close to room temperature seems to arise from thermally activated reverse internal conversion. As such a process does not involve any spin flip, it should be governed by the same large matrix elements contributing to the well known fast internal conversion downwards in energy. After the excited triplet configuration  $^3A$  would have been reached by reverse internal conversion, a fast rISC process towards the lowest singlet  $^1CT$  could occur without further activation energy. The lineshape of delayed fluorescence and its average energy (see Fig. 8b) depend only weakly on temperature, so that it seems natural to assign the radiative recombination process to  $S_1 \rightarrow S_0$  for all temperatures.

Other high-temperature processes, involving e.g. triplet migration or charge separation between adjacent DMAC-MB emitters and subsequent recombination from intermolecular CT transitions seem less likely because they should involve much smaller thermal activation energies with respect to the data analysis in Fig. 4b.

## Emission at long delays

Close to room temperature, at long delays (beyond 200  $\mu s$ , see Fig. 8a), the relative contribution of a relaxed  $^3CT$  triplet population still able to promote delayed fluorescence via TADF diminishes, and instead, a further contribution to fluorescence centered around 2.12 eV growth in relative strength.

Among the possible phosphorescence transitions in Fig. 14, the calculated transition  $^3A \rightarrow S_0$  at 2.54 eV is red-shifted by 0.18 eV with respect to the CT transition  $^3CT \rightarrow S_0$ . As discussed previously in Sec. , the observed Stokes shift on the  $^1CT$  potential surface is about 1.37 times larger than the calculated value of 0.67 eV derived from TD-DFT with the optimally tuned range separated hybrid. Rescaling the deformation energy at the  $^3A$

potential minimum by the same amount, the calculated Stokes shift between  $S_0$  and  ${}^3A$  geometries would increase from 0.98 eV to 1.34 eV, placing the phosphorescence transition at 2.18 eV, in reasonable agreement with the observed late fluorescence channel close to room temperature.

As demonstrated by its substantial contribution to delayed fluorescence close to room temperature derived from Fig. 4, most of the reverse internal conversion  ${}^3CT \rightarrow {}^3A$  seems to be followed by fast barrierless rISC process,  ${}^3A \rightarrow S_1$ . Hence, only rather few  ${}^3A$  triplet states can thermalize towards the respective potential minimum without converting to  $S_1$  via a rISC process, so that a significant fraction of  ${}^3A \rightarrow S_0$  phosphorescence emerges only at quite late delay times.

### Triplet-triplet annihilation

In Figs. 2 and 3, the seemingly algebraic decay at late delay times gives clear evidence for TTA. According to the Franck-Condon principle, energy conservation has to be evaluated at frozen relaxed  $T_1$  geometries, so that



requires an excited singlet  $S_n$  fulfilling a resonance condition between different transition energies

$$S_n \leftarrow S_0 \approx 2(T_1 \rightarrow S_0) \tag{49}$$

in a molecular geometry corresponding to the relaxed  $T_1$  potential minimum. Depending on the system under study, this may require different excited singlets  $S_n$ . Among the polyacene series, anthracene allows for resonant excitation of  $S_1$  via TTA,<sup>68</sup> whereas in pentacene, the lowest excited singlet lies slightly too high, favouring instead the reverse process, i.e. singlet fission resulting in two  $T_1$  triplets. In specific systems with particularly weak  $S_1 \rightarrow S_0$

fluorescence like 4,6,8-trimethylazulene, other emission channels like  $S_2 \rightarrow S_0$  may be in resonance with TTA.<sup>69</sup> Even in the more common case where TTA results in fluorescence from the lowest excited singlet  $S_1$ , TTA towards an excited state  $S_n$  may be followed by fast internal conversion  $S_n \rightarrow S_1$ , so that the resonance condition eq.(49) for  $S_n$  can be reconciled with a lowest excited singlet  $S_1$  far below.

In our model system DMAC-MB, symmetry constraints within the point group  $C_s$  demonstrate that the lowest triplet  $T_1$  corresponds to a CT state transforming according to the  $a''$  representation. Therefore, TTA has to end up in an electronic configuration transforming according to the  $a'$  representation. For a final state with singlet spin configuration, this reads

$$T_1(a'') + T_1(a'') \rightarrow S_0(a') + S_n(a'), \quad (50)$$

a requirement excluding  $S_0(a') + S_1(a'')$  and any other combination  $S_0(a') + S_n(a'')$  as possible final states. Furthermore, energy conservation dictates a possible range for the energy of the final state  $S_n$ . Starting with an average observed fluorescence transition from the lowest excited singlet configuration  ${}^1\text{CT} \rightarrow S_0$  at 2.46 eV, the respective triplet transition would be placed at 2.44 eV by subtracting the calculated singlet-triplet splitting of  $\Delta_{\text{ST}} = 0.02$  eV. According to eq. (49), this would correspond to a final state  $S_n$  with a transition energy  $S_n \leftarrow S_0$  around 4.88 eV. The best matching  $S_n$  can be obtained from transition energies calculated with TD-DFT in optimized  $T_1$  geometry, giving  $S_6(a') \leftarrow S_0(a')$  at 4.84 eV as an excellent candidate. This excited singlet involves mainly a transition on the acceptor from a mixture between the  $\pi_{\text{A}}$  orbitals HOMO-5 and HOMO-4 depicted in Fig. 11 to the  $\pi_{\text{A}}^*$  LUMO.

After resonant TTA towards  $S_6(a')$ , fast internal conversion  $S_6(a') \rightarrow S_1(a'')$  releases about 2.42 eV of thermal energy, raising the temperature of the molecule by about  $\Delta T = 400$  K. Such a huge amount of heating may quite well contribute to photochemical degradation of blue TADF emitters allowing for resonant population of high lying excited singlets

via TTA.

## Conclusion

In the present work, we have investigated a prototypical small TADF emitter with time-resolved spectroscopy, photoluminescence excitation, and density functional theory relying on an optimally tuned long-range corrected hybrid functional. By construction, this emitter shows intense TADF, involving the expected thermal activation via rISC,  ${}^3\text{CT} \rightarrow {}^1\text{CT}$ , but also an indirect process, combining reverse internal conversion  ${}^3\text{CT} \rightarrow {}^3\text{A}$  with subsequent barrierless rISC  ${}^3\text{A} \rightarrow {}^1\text{CT}$ . The same rIC process is also responsible for a late contribution to phosphorescence, assigned to radiative recombination  ${}^3\text{A} \rightarrow S_0$ . The seemingly algebraic decay at late delays gives clear evidence for triplet-triplet annihilation, involving a rather unusual resonance condition,  $T_1(a'') + T_1(a'') \rightarrow S_0(a') + S_6(a')$ .

An assignment of this large variety of phenomena requires a DFT method which is able to reproduce CT transitions with a rather small error margin. In sharp contrast to the popular global hybrid B3LYP, its optimally tuned long-range corrected generalization LC-B3LYP allows to assign the energies of the lowest absorption bands quantitatively, achieving a similar precision for both CT excitations and donor excitations. Detailed DFT studies of various excited potential minima reveal that the dominating fluorescence feature arises from a mirror-symmetric  $S_1$  minimum, whereas TADF from the  $T_1$  potential towards  $S_1$  is promoted through the quite small singlet-triplet splitting occurring in similar geometries. Embedding of the TADF emitter into a rather rigid polymer matrix and the impact of the surrounding polarizable medium onto the lowest triplet potential landscape seems to suppress deformations involving a substantial distortion of the dihedral angle between donor and acceptor away from mirror symmetry. Due to the very high excited singlets arising from TTA, excited potential surfaces have to be tracked up to about 5 eV above the electronic ground state. The enormous amount of excess energy generated by such resonant TTA

processes could contribute to photochemical degradation of our model compound and similar TADF systems.

As observed already for other systems, time-dependent DFT may significantly underestimate excited state deformations and the resulting Stokes shift. This deficiency still occurs for the long-range corrected hybrid promoted in the present work, so that we suspect that it is a more general feature of excited state potential surfaces derived from time-dependent DFT.

## Acknowledgement

This work has received funding from the Horizon 2020 programme within the project PHEBE (grant agreement 641725). Computational resources provided by the Centre for Information Services and High Performance Computing (ZIH) of TU Dresden are gratefully acknowledged.

## References

- (1) Tang, C. W.; VanSlyke, S. A.; Chen, C. H. Electroluminescence of doped organic thin films. J. Appl. Phys. **1989**, 65, 3610–3616.
- (2) Rothberg, L. J.; Lovinger, A. J. Status of and prospects for organic electroluminescence. J. Mater. Res. **1996**, 11, 3174–3187.
- (3) Baldo, M. A.; O’Brien, D. F.; You, Y.; Shoustikov, A.; Sibley, S.; Thompson, M. E.; Forrest, S. R. Highly efficient phosphorescent emission from organic electroluminescent devices. Nature **1998**, 395, 151–154.
- (4) Reineke, S.; Lindner, F.; Schwartz, G.; Seidler, N.; Walzer, K.; Lüssem, B.; Leo, K. White organic light-emitting diodes with fluorescent tube efficiency. Nature **2009**, 459, 234–238.

- (5) Parker, C. A.; Hatchard, C. G. Triplet-singlet emission in fluid solutions. Phosphorescence of eosin. Trans. Faraday Soc. **1961**, 57, 1894–1904.
- (6) Blasse, G.; McMillin, D. R. On the luminescence of bis (triphenylphosphine) phenanthroline copper (I). Chem. Phys. Lett. **1980**, 70, 1 – 3.
- (7) Palmer, C.; McMillin, D. R. Singlets, Triplets, and Exciplexes: Complex, Temperature-Dependent Emissions from Cu(dmp)(PPh<sub>3</sub>)<sub>2</sub><sup>+</sup> and Cu(phen)(PPh<sub>3</sub>)<sub>2</sub><sup>+</sup> in Solution. Inorg. Chem. **1987**, 26, 3837–3840.
- (8) Endo, A.; Ogasawara, M.; Takahashi, A.; Yokoyama, D.; Kato, Y.; Adachi, C. Thermally Activated Delayed Fluorescence from Sn<sup>4+</sup>-Porphyrin Complexes and Their Application to Organic Light Emitting Diodes – A Novel Mechanism for Electroluminescence. Adv. Mater. **2009**, 21, 4802–4806.
- (9) Czerwieńiec, R.; Yu, J.; Yersin, H. Blue-Light Emission of Cu(I) Complexes and Singlet Harvesting. Inorg. Chem. **2011**, 50, 8293–8301.
- (10) Osawa, M.; Kawata, I.; Ishii, R.; Igawa, S.; Hashimoto, M.; Hoshino, M. Application of neutral d<sup>10</sup> coinage metal complexes with an anionic bidentate ligand in delayed fluorescence-type organic light-emitting diodes. J. Mater. Chem. C **2013**, 1, 4375–4383.
- (11) Uoyama, H.; Goushi, K.; Shizu, K.; Nomura, H.; Adachi, C. Highly efficient organic light-emitting diodes from delayed fluorescence. Nature **2012**, 492, 234–238.
- (12) Laurent, A. D.; Jacquemin, D. TD-DFT benchmarks: A review. Int. J. Quantum Chem. **2013**, 113, 2019–2039.
- (13) Becke, A. D. Density-functional thermochemistry. III. The role of exact exchange. J. Chem. Phys. **1993**, 98, 5648–5652.
- (14) Dreuw, A.; Weisman, J. L.; Head-Gordon, M. Long-range charge-transfer excited states

- in time-dependent density functional theory require non-local exchange. J. Chem. Phys. **2003**, 119, 2943–2946.
- (15) Huang, S.; Zhang, Q.; Shiota, Y.; Nakagawa, T.; Kuwabara, K.; Yoshizawa, K.; Adachi, C. Computational Prediction for Singlet- and Triplet-Transition Energies of Charge-Transfer Compounds. J. Chem. Theory Comput. **2013**, 9, 3872–3877.
- (16) Zhang, Q.; Kuwabara, H.; Potscavage, W. J.; Huang, S.; Hatae, Y.; Shibata, T.; Adachi, C. Anthraquinone-Based Intramolecular Charge-Transfer Compounds: Computational Molecular Design, Thermally Activated Delayed Fluorescence, and Highly Efficient Red Electroluminescence. J. Am. Chem. Soc. **2014**, 136, 18070–18081.
- (17) Gibson, J.; Monkman, A. P.; Penfold, T. J. The Importance of Vibronic Coupling for Efficient Reverse Intersystem Crossing in Thermally Activated Delayed Fluorescence Molecules. ChemPhysChem **2016**, 17, 2956–2961.
- (18) Iikura, H.; Tsuneda, T.; Yanai, T.; Hirao, K. A long-range correction scheme for generalized-gradient-approximation exchange functionals. J. Chem. Phys. **2001**, 115, 3540–3544.
- (19) Tawada, Y.; Tsuneda, T.; Yanagisawa, S.; Yanai, T.; Hirao, K. A long-range-corrected time-dependent density functional theory. J. Chem. Phys. **2004**, 120, 8425–8433.
- (20) Baer, R.; Neuhauser, D. Density Functional Theory with Correct Long-Range Asymptotic Behavior. Phys. Rev. Lett. **2005**, 94, 043002.
- (21) Yanai, T.; Tew, D. P.; Handy, N. C. A new hybrid exchange-correlation functional using the Coulomb-attenuating method (CAM-B3LYP). Chem. Phys. Lett. **2004**, 393, 51–57.
- (22) Stein, T.; Kronik, L.; Baer, R. Reliable Prediction of Charge Transfer Excitations in

- Molecular Complexes Using Time-Dependent Density Functional Theory. J. Am. Chem. Soc. **2009**, 131, 2818–2820.
- (23) Tanaka, H.; Shizu, K.; Nakanotani, H.; Adachi, C. Dual Intramolecular Charge-Transfer Fluorescence Derived from a Phenothiazine-Triphenyltriazine Derivative. J. Phys. Chem. C **2014**, 118, 15985–15994.
- (24) Sun, H.; Zhong, C.; Brédas, J.-L. Reliable Prediction with Tuned Range-Separated Functionals of the Singlet-Triplet Gap in Organic Emitters for Thermally Activated Delayed Fluorescence. J. Chem. Theory Comput. **2015**, 11, 3851–3858.
- (25) Shu, Y.; Levine, B. G. Simulated evolution of fluorophores for light emitting diodes. J. Chem. Phys. **2015**, 142, 104104.
- (26) Penfold, T. J. On Predicting the Excited-State Properties of Thermally Activated Delayed Fluorescence Emitters. J. Phys. Chem. C **2015**, 119, 13535–13544.
- (27) Tian, X.; Sun, H.; Zhang, Q.; Adachi, C. Theoretical prediction for transition energies of thermally activated delayed fluorescence molecules. Chin. Chem. Lett. **2016**, 27, 1445 – 1452.
- (28) Ward, J. S.; Nobuyasu, R. S.; Fox, M. A.; Batsanov, A. S.; Santos, J.; Dias, F. B.; Bryce, M. R. Bond Rotations and Heteroatom Effects in Donor-Acceptor-Donor Molecules: Implications for Thermally Activated Delayed Fluorescence and Room Temperature Phosphorescence. J. Org. Chem. **2018**, 83, 14431–14442.
- (29) Penfold, T. J.; Dias, F. B.; Monkman, A. P. The theory of thermally activated delayed fluorescence for organic light emitting diodes. Chem. Commun. **2018**, 54, 3926–3935.
- (30) Lv, L.; Yuan, K.; Zhu, Y.; Zuo, G.; Wang, Y. Investigation of Conversion and Decay Processes in Thermally Activated Delayed Fluorescence Copper(I) Molecular Crystal:

- Theoretical Estimations from an ONIOM Approach Combined with the Tuned Range-Separated Density Functional Theory. J. Phys. Chem. A **2019**, 123, 2080–2090.
- (31) Alipour, M.; Safari, Z. Photophysics of OLED Materials with Emitters Exhibiting Thermally Activated Delayed Fluorescence and Used in Hole/Electron Transporting Layer from Optimally Tuned Range-Separated Density Functional Theory. J. Phys. Chem. C **2019**, 123, 746–761.
- (32) Loudon, R. The Quantum Theory of Light; Clarendon, Oxford, 1983.
- (33) Zhang, Q.; Li, B.; Huang, S.; Nomura, H.; Tanaka, H.; Adachi, C. Efficient blue organic light-emitting diodes employing thermally activated delayed fluorescence. Nature Photonics **2014**, 8, 326–332.
- (34) Kim, J. H.; Hwang, S.-H.; Song, W.; Lee, J. Y. Acridine modified dibenzothiophene derivatives as high triplet energy host materials for blue phosphorescent organic light-emitting diodes. Dyes and Pigments **2015**, 122, 103–108.
- (35) Lee, I.; Lee, J. Y. Molecular design of deep blue fluorescent emitters with 20% external quantum efficiency and narrow emission spectrum. Organ. Electron. **2016**, 29, 160–164.
- (36) Hellwinkel, D.; Schmidt, W. Modifizierte Tetrahelicen-Systeme, III. Zweifach ortho-verbrückte Triphenylamin-Derivate. Chem. Ber. **1980**, 113, 358–384.
- (37) Andrew, T. L.; Swager, T. M. Detection of Explosives via Photolytic Cleavage of Nitroesters and Nitramines. J. Org. Chem. **2011**, 76, 2976–2993.
- (38) Matoušek, V.; Pietrasiak, E.; Schwenk, R.; Togni, A. One-Pot Synthesis of Hypervalent Iodine Reagents for Electrophilic Trifluoromethylation. J. Org. Chem. **2013**, 78, 6763–6768.
- (39) These data can be obtained free of charge from [www.ccdc.cam.ac.uk/data\\_request/cif](http://www.ccdc.cam.ac.uk/data_request/cif)

(or from the Cambridge Crystallographic Data Centre (CCDC), 12 Union Road, Cambridge CB2 1EZ; fax: 44(0) 1223 336 033; email: deposit@ccdc.cam.ac.uk).

- (40) de Mello, J. C.; Wittmann, H. F.; Friend, R. H. An improved experimental determination of external photoluminescence quantum efficiency. Adv. Mater. **1997**, 9, 230–232.
- (41) Rothe, C.; Monkman, A. P. Triplet exciton migration in a conjugated polyfluorene. Phys. Rev. B **2003**, 68, 075208.
- (42) Jankus, V.; Winscom, C.; Monkman, A. P. Dynamics of triplet migration in films of N, N'-diphenyl-N, N'-bis(1-naphthyl)-1, 1'-biphenyl-4, 4''-diamine. J. Phys.: Condens. Matter **2010**, 22, 185802.
- (43) Dias, F. D.; Penfold, T. J.; Monkman, A. P. Photophysics of thermally activated delayed fluorescence molecules. Methods Appl. Fluoresc. **2017**, 5, 012001.
- (44) Dias, F. B.; Bourdakos, K. N.; Jankus, V.; Moss, K. C.; Kamtekar, K. T.; Bhalla, V.; Santos, J.; Bryce, M. R.; Monkman, A. P. Triplet Harvesting with 100% Efficiency by Way of Thermally Activated Delayed Fluorescence in Charge Transfer OLED Emitters. Adv. Mater. **2013**, 25, 3707–3714.
- (45) Strickler, S. J.; Berg, R. A. Relationship between Absorption Intensity and Fluorescence Lifetime of Molecules. J. Chem. Phys. **1962**, 37, 814–822.
- (46) Huang, K.; Rhys, A.; Mott, N. F. Theory of light absorption and non-radiative transitions in F-centres. Proc. Roy. Soc. A **1950**, 204, 406–423.
- (47) Scholz, R.; Kobitski, A.; Kampen, T.; Schreiber, M.; Zahn, D.; Jungnickel, G.; Elstner, M.; Sternberg, M.; Frauenheim, T. Resonant Raman spectroscopy of 3,4,9,10-perylene-tetracarboxylic-dianhydride epitaxial films. Phys. Rev. B **2000**, 61, 13659–13669.

- (48) Dierksen, M.; Grimme, S. Density functional calculations of the vibronic structure of electronic absorption spectra. J. Chem. Phys. **2004**, 120, 3544–3554.
- (49) Kytka, M.; Gisslen, L.; Gerlach, A.; Heinemeyer, U.; Kováč, J.; Scholz, R.; Schreiber, F. Optical spectra obtained from amorphous films of rubrene: Evidence for predominance of twisted isomer. J. Chem. Phys. **2009**, 130, 214507.
- (50) Moral, M.; Muccioli, L.; Son, W.-J.; Olivier, Y.; Sancho-García, J. C. Theoretical Rationalization of the Singlet-Triplet Gap in OLEDs Materials: Impact of Charge-Transfer Character. J. Chem. Theory and Computat. **2015**, 11, 168–177.
- (51) Perdew, J. P.; Levy, M. Physical Content of the Exact Kohn-Sham Orbital Energies: Band Gaps and Derivative Discontinuities. Phys. Rev. Lett. **1983**, 51, 1884–1887.
- (52) Sham, L. J.; Schlüter, M. Density-Functional Theory of the Energy Gap. Phys. Rev. Lett. **1983**, 51, 1888–1891.
- (53) Bauschlicher, C. W. A comparison of the accuracy of different functionals. Chem. Phys. Lett. **1995**, 246, 40 – 44.
- (54) Yoshida, H.; Takeda, K.; Okamura, J.; Ehara, A.; Matsuura, H. A New Approach to Vibrational Analysis of Large Molecules by Density Functional Theory: Wavenumber-Linear Scaling Method. J. Phys. Chem. A **2002**, 106, 3580–3586.
- (55) Jacquemin, D.; Wathelet, V.; Perpète, E. A.; Adamo, C. Extensive TD-DFT Benchmark: Singlet-Excited States of Organic Molecules. J. Chem. Theory Comput. **2009**, 5, 2420–2435.
- (56) Jacquemin, D.; Perpète, E. A.; Ciofini, I.; Adamo, C.; Valero, R.; Zhao, Y.; Truhlar, D. G. On the Performances of the M06 Family of Density Functionals for Electronic Excitation Energies. J. Chem. Theory Comput. **2010**, 6, 2071–2085.

- (57) Leang, S. S.; Zahariev, F.; Gordon, M. S. Benchmarking the performance of time-dependent density functional methods. J. Chem. Phys. **2012**, 136, 104101.
- (58) Livshits, E.; Baer, R. A well-tempered density functional theory of electrons in molecules. Phys. Chem. Chem. Phys. **2007**, 9, 2932–2941.
- (59) Refaely-Abramson, S.; Baer, R.; Kronik, L. Fundamental and excitation gaps in molecules of relevance for organic photovoltaics from an optimally tuned range-separated hybrid functional. Phys. Rev. B **2011**, 84, 075144.
- (60) Kronik, L.; Stein, T.; Refaely-Abramson, S.; Baer, R. Excitation Gaps of Finite-Sized Systems from Optimally Tuned Range-Separated Hybrid Functionals. J. Chem. Theory Comput. **2012**, 8, 1515–1531.
- (61) Valiev, M.; Bylaska, E.; Govind, N.; Kowalski, K.; Straatsma, T.; Dam, H. V.; Wang, D.; Nieplocha, J.; Apra, E.; Windus, T.; de Jong, W. NWChem: A comprehensive and scalable open-source solution for large scale molecular simulations. Comput. Phys. Commun. **2010**, 181, 1477 – 1489.
- (62) Refaely-Abramson, S.; Sharifzadeh, S.; Jain, M.; Baer, R.; Neaton, J. B.; Kronik, L. Gap renormalization of molecular crystals from density-functional theory. Phys. Rev. B **2013**, 88, 081204.
- (63) Cucchi, M.; Matulaitis, T.; Kukhta, N. A.; Grazulevicius, J. V.; Reineke, S.; Scholz, R. Influence of the Dielectric Constant around an Emitter on Its Delayed Fluorescence. Phys. Rev. Applied **2019**, 12, 044021.
- (64) Duan, Y.-C.; Wen, L.-L.; Gao, Y.; Wu, Y.; Zhao, L.; Geng, Y.; Shan, G.-G.; Zhang, M.; Su, Z.-M. Fluorescence, Phosphorescence, or Delayed Fluorescence? – A Theoretical Exploration on the Reason Why a Series of Similar Organic Molecules Exhibit Different Luminescence Types. J. Phys. Chem. C **2018**, 122, 23091–23101.

- (65) Gisslén, L.; Scholz, R. Crystallochromy of perylene pigments: Interference between Frenkel excitons and charge-transfer states. Phys. Rev. B **2009**, 80, 115309.
- (66) Föller, J.; Kleinschmidt, M.; Marian, C. M. Phosphorescence or Thermally Activated Delayed Fluorescence? Intersystem Crossing and Radiative Rate Constants of a Three-Coordinate Copper(I) Complex Determined by Quantum-Chemical Methods. Inorg. Chem. **2016**, 55, 7508–7516.
- (67) Lyskov, I.; Marian, C. M. Climbing up the Ladder: Intermediate Triplet States Promote the Reverse Intersystem Crossing in the Efficient TADF Emitter ACRSA. J. Phys. Chem. C **2017**, 121, 21145–21153.
- (68) Kepler, R. G.; Caris, J. C.; Avakian, P.; Abramson, E. Triplet excitons and Delayed Fluorescence in Anthracene Crystals. Phys. Rev. Lett. **1963**, 10, 400–402.
- (69) Klemp, D.; Nickel, B. Delayed fluorescence  $S_2 \rightarrow S_0$  from 4,6,8-trimethylazulene due to homo-triplet-triplet annihilation. Chem. Phys. Lett. **1983**, 97, 66 – 71.